POLITECNICO DI MILANO

Faculty of Engineering

Department of Chemistry, Materials

and Chemical Engineering "Giulio Natta"

Piezoresistivity of Graphene

Supervisor: **Prof. Herre van der Zant (TUDelft)**

Co-supervisors: **Prof. Matteo Tommasini (Politecnico di Milano)**

Dr. Menno Poot (TUDelft)

Master Thesis by:

Elham Khatibi **Matr. 737093**

Academic Year: 2010/2011

List of Contents:

List of Figures:

List of Tables

Abstract

Graphene is the thinnest known material, which gathered a lot of attention after its discovery because of unique electrical and mechanical properties such as high stiffness and electron mobility. Besides, the small size and mass of graphene make it an ideal candidate for nanoelectromechanical systems (NEMS), which offer potential for new applications such as single atom mass sensors.

In addition to the mentioned features, the interplay between mechanical and electrical properties of graphene is an interesting functionality for designing NEMS. This interplay is called “piezoresistivity” and is investigated by gauge factor (GF) which is the ratio of relative changes in the electrical resistance to the applied mechanical strain.

In this thesis we report for the first time the experimental study of the piezoresistivity in few layer graphene “nanodrums”, that are suspended flakes over circular holes. We measure the electrical resistance of the flake while the flake is deformed by means of the force-distance measurements by an atomic force microscopy (AFM) under ambient condition. Furthermore, the analysis of the experimental data required the writing of a program in Matlab to merge the results of the AFM and electrical measurements. By this program the measured force-distance curves and changes in the electrical resistance while the AFM tip is deforming the flake are plotted. In addition to that the spatial profile of the compliance of the flake is plotted to show the pattern of the deformability of the flake. Moreover, the spatial profile of the changes in the electrical resistance of the flake while the tip is pushing the flake and the flake is deformed is plotted. This factor gives information about the changes in the GF and the piezoresistivity of the graphene flakes.

The results proved that our method to use AFM under ambient condition as a measurement tool can be used to derive information on the piezoresistive behavior of graphene. According to the results at the center of the hole the flake is more easily deflected than the edges. Moreover, the deformation of the drums through AFM affects the electrical resistance of the flake (by approximately 10%) and it shows that graphene illustrates piezoresistive behavior in practice. This is a promising prospect for applications of the graphene nanodrum as the sensor of very small mass (individual molecules) or pressure changes in NEMS.

Sommario

Il grafene, l'unico materiale conosciuto in forma di singolo strato atomico, ha attratto molta attenzione fin dalla sua scoperta grazie alle proprietà elettriche e meccaniche uniche (elevato modulo e mobilità di carica).

Inoltre, la ridotta massa di un flake di grafene e le sue ridotte dimensioni ne fanno un candidato ideale per sistemi nano-elettromeccanici (NEMS) che potrebbero condurre allo sviluppo di nanosensori di massa e pressione.

In particolare l'accoppiamento tra le proprietà meccaniche ed elettriche del grafene (la piezoresistività) rappresenta il parametro fisico che può essere utilmente sfruttato nella costruzione di dispositivi alla scala nanometrica.

In questa tesi si riporta uno studio sperimentale originale della piezoresistività di "nanotamburi" di grafene a pochi strati. Tali nanotamburi sono costituiti da flake di grafene sospesi su buchi circolari ricavati su substrati di silicio.

Nel corso della tesi è stata misurata (a temperatura e pressione ambiente) la variazione della resistenza della membrana di grafene del nanotamburo sotto l'azione deformante della punta di un AFM. L'analisi dei dati sperimentali ha richiesto la scrittura di un programma Matlab per elaborare ed unire i risultati delle misure simultanee AFM ed elettrica. Tale programma permette di visualizzare sia il profilo spaziale della deformazione della membrana grafenica del nanotamburo (misurata con l'AFM) che quello della resistenza elettrica della membrana. In questo modo è possibile caratterizzare esaustivamente il comportamento piezoresistivo della membrana grafenica del nanotamburo. I risultati delle misure effettuate mostrano che il centro della membrana è più facilmente deformato dei suoi bordi, come atteso. Sotto l'azione della punta AFM si misurano variazioni dell'ordine del 10% nella resistenza elettrica della membrana. Questo rappresenta un risultato promettente nei confronti della possibile realizzazione di nanosensori di masse ridottissime (singole molecole) o di piccoli cambiamenti di pressione.

Chapter 1

Introduction

Nanoelectromechanical systems (NEMS) are interesting candidates to revolutionize measurements of i.e. extremely small displacements and week forces, with their small mass and nano size [1]. These systems are continuing of the microelectromechanical systems (MEMS) that are made by integrated-circuit technology in nanometer scale. The scaling down of these devices increases their resonance frequency and decreases their mass [2]. Such unique attributes of NEMS offer immense potential for new applications and fundamental measurements such as single-atom mass sensing and mechanical computing [1, 2]. To take full advantage of these systems we will have to stretch our imaginations, as well as our current methods and mindset in nanoscale science and technology. By today, many scientists have merged the most important semiconductor materials such as silicon, germanium, and carbon allotropes with NEMS and achieved systems that host intriguing attributes [2].

In current work we have focused on NEMS made from one of the carbon allotropes called graphene. Graphene with a 2D structure which once was believed cannot exist, is nowadays considered as one of the most promising materials for the future of electronics at the nanoscale. The reason is its rich variety of physical features of graphene such as high carrier mobility and quantum hall effect. Moreover, motivated by graphene's lightness and stiffness and the rather flexible electronic character under stress, the interplay between mechanical and electrical properties of graphene became another direction of research beyond the realm of purely electronic or mechanical studies in which such features are essential functionalities for building up low-cost NEMS [3].

Piezoresistivity which is the change in the electrical property of the material by changing its mechanical status is an interesting property to be applied in NEMS. In recent years some researchers have studied the piezoresistivity of some carbon allotropes theoretically and experimentally such as carbon nanotube [4, 5]. But in the case of graphene only theoretical studies have been done to predict its electromechanical behavior [3, 6] and no experiment have been reported by the time of this research.

In this research we have studies for the first time the piezoresistive behavior of graphene experimentally. The samples are made by suspending the graphene flakes on top of a hole in the form of nanodrums. In order to investigate the piezoresistive behavior some electrical settings are added to an atomic force microscopy (AFM) to let us measure the electrical resistance of the flake. Then the drums are deformed by the AFM tip and meanwhile their electrical resistance is

measured. Later a program is made in MATLAB to merge the measured mechanical and electrical results and give the profile of the compliance and change in the electrical properties over the surface.

In this thesis, first an introduction is given about NEMS, carbon materials and specifically graphene and piezoresistivity in this chapter. Then in chapter 2 the nanomechanics of the nanodrums is studied and some researches that have been done in this field are reported. In chapter 3 the fabrication of samples are explained. Later in chapter 4, the methods and settings used for measurements are discussed. Then in chapter 5 the results are shown and discussed, and at the end in chapter 6 the conclusion of this research is explained.

1.1. Nanoelectromechanical Systems

Nanoelectromechanical systems or NEMS are defined as i.e. the mechanics, sensors, computers and electronics that are in the nanoscale. But they are not just downscaled microsystems. They provide completely new functionalities since they offer interface to the physical world and promising applications in chemistry, microbiology, medicine and nanotechnology [39]. In this size regime, it is possible to attain the extremely high fundamental frequencies and mechanical quality factors, the force sensitivities at the attonewton level the mass sensitivity at the level of individual molecules [7].

In general, an electromechanical system consists of a mechanical element and some transducers. The mechanical element either deflects or vibrates in response to an applied force. The transducers convert mechanical energy into electrical or optical signals and vice versa [7]. Mainly there are two types of response: the element simply deflects under an applied force or some changes appear in its amplitude of oscillation. Usually the responses are detected by an output or readout transducer which is distinct from the input one [1].

Ordinarily there are two approaches in fabrication of NEMS. One technique is called the top-down fabrication, in which the pattern of a nanoscale structures is copied on a resist mask, and then it is transferred to a larger structure by etching or depositing another material. The patterning is usually done by electron-beam lithography (E-beam). Modern fabricated devices with this method can have dimensions less than 100 nanometers. The second approach is the bottom-up technique. In this method the small structures from nature are used to build or

assemble devices. This technique allows building the devices with true nanometer dimensions. Devices made from carbon material are made by this method.

The progress of the mentioned fabrication techniques allows having nanoscale devices even around 10nm. The devices in this size offer novel and fascinating opportunities for sensing and measurements such as:

- It is possible to have nanoscale resonators with fundamental frequencies above 10GHz. such high frequency opens exciting possibilities; i.e. ultralow-power mechanical signal processing at the microwave frequencies and fast scanning probe microscopes [1].

- Nanoscale devices dissipate very little energy which is evaluated by their quality factor (Q). A high Q value makes both the resonant and the deflection sensors very sensitive to the applied forces. It is done by suppressing the random mechanical fluctuations. Indeed, this sensitivity appears to reach to the quantum limit [1].

- NEMS can be fabricated from a large variety of materials including silicon, gallium arsenide and etc. As a result, all the main components of the electronic and mechanical systems can be patterned on the same chip. Such ability solves many problems of the fabrication and alignment of the components [1].

By this time it may appear that it is easy to build NEMS. But to take a full advantage of these systems we will have to stretch our imaginations as well as our current methods and nanoscale science and technology. At the moment there are three main challenges that must be addressed before the full potential of NEMS can be realized: communicating signals from the nanoscale to macroscopic world, understanding and controlling the mesoscopic mechanisms and developing methods for reproducible and routine nanofabrication [1].

Besides the mentioned materials, new materials such as carbon nanotube and graphene which own novel physical properties promise to play a significant role in overcoming the classic downscaling problems [8]. In addition to that carbon with a variety of crystalline structures and properties is an interesting engineering material. These properties make it a good candidate for different physical, chemical, mechanical and electrical applications. Carbon based Microelectromechanical Systems (MEMS) and Nanoelectromechanical Systems (NEMS), with sizes ranging from millimeter to nanometer, can provide progress, alone or in combination with Si and other materials for microelectronics, nanoelectronics, sensors, miniaturized power systems [9].

On the whole, such attributes make NEMS suitable for technological applications such as the ultrafast sensors, actuators and signal processing components. They are clearly destined to provide much of the crucial scientific and engineering foundations that will underline future nanotechnology.

1.2. Graphene

Carbon allotropes demonstrate unusual and complicated behavior by forming different structures; for example diamond, graphite and recently discovered fullerenes, carbon nanotube and graphene which are focused for many researches by physicist and chemists. Graphene is a flat monolayer of carbon atoms tightly bound together in a two-dimensional honeycomb lattice. It is considered to be the building block of the other carbon allotropes including fullerenes (zero-dimensional), carbon nanotube (one-dimensional) and graphite (three-dimensional) [10]. All these allotropes of carbon are depicted in Fig. 1.1.

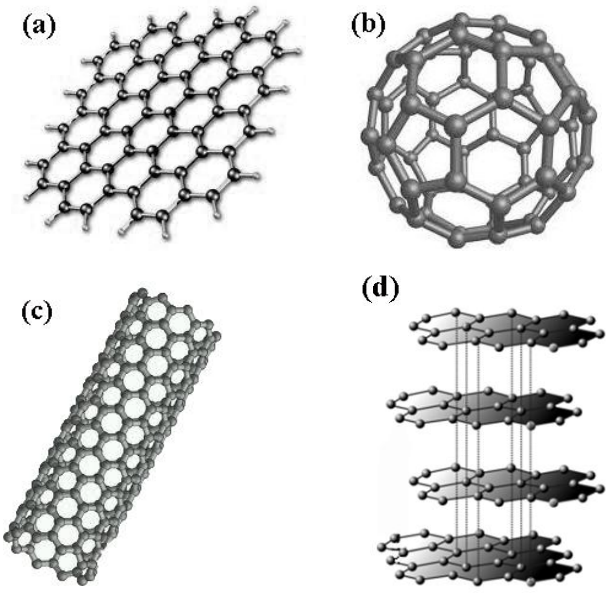

Figure 1.1- Schematic structure of (a) [1] graphene as the building block of other carbon allotropes including: (b) [2] fullerene (0D), (c) [3] carbon nanotube (1D) and (d) [4]graphite (3D).

[1] Ref. :http://www.mc2quantum.com
[2] Ref.: http://www.suite101.com/view_image.cfm/799781
[3] Ref.: http://www.ati.surrey.ac.uk/topics?topic_id=32&level=1
[4] Ref.: http://mrsec.wisc.edu/Edetc/nanoquest/carbon/index.html

At the beginning any attempts for synthesizing such two-dimensional atomic crystal have usually failed, leading instead to nanometer-size crystallites [11]. During synthesis the large perimeter-to-surface ratios of graphene nucleation sites, causes the structure to collapse into other carbon allotropes [12]. It was not surprising since it was believed that two-dimensional crystals cannot exist because they are thermodynamically unstable [13- 15]. According to the Landau [16] and Peierls [8] theorem, the thermal fluctuations displace atoms in a distance comparable to the interatomic distances at any finite temperature. Consequently, there should be no long-range order in the low-dimensional crystal lattices. Besides, it was observed that melting temperature of thin films rapidly decrease when their thickness decrease to the dozens of atomic layers, and they become unstable [17-19].

In 2004 the discovery of graphene revealed the fact that 2D crystals do exist and moreover they exhibit high crystal quality [20-23]. Graphene was first observed experimentally by a simple approach based on micromechanical cleavage of bulk graphite [10, 24]. In this method which is called the mechanical exfoliation, bulk graphite is peeled repeatedly with adhesive tape to get the thinnest flakes [20]. Using this top-down approach helped the researchers to avoid all the issues with the stability of small crystallites [12].

There is an idea which says 2D crystals are intrinsically stable because of the existence of some ripples in the third dimension [25]. Such warping leads to gain in elastic energy but suppress the thermal vibrations, which above a certain temperature can minimize the total free energy. These ripples are observed also in graphene and they play an important role in its electronic properties [26].

The mechanical exfoliation method makes it possible to have high quality and large (up to 100μm in size [27]) samples. The qualities of samples are so good that ballistic transport [28] and quantum Hall effect [22, 28] can be observed easily. That's why among two-dimensional materials, graphene has attracted a great attention since its discovery. In addition to such unique electrical properties, it demonstrates interesting mechanical properties such as high mechanical strength and young module. Such properties make it an ideal material for NEMS applications such as force, position and mass sensors [29, 30].

Today, still other techniques are required to provide graphene industrially. Among the promising candidate, exfoliation of intercalated graphitic compounds [31, 32] and Si sublimation from SiC substrates [33, 34] have the potential, to be investigated. In the first methods the

graphene layers are separated by intercalating molecules into bulk graphite. As this method is uncontrollable it has not attracted much interest [31]. In the second method the production of epitaxial graphene is based on laser-induced surface decomposition of the Si-rich face of a SiC single-crystal. The results of this method show that the thickness can be controlled up to single layer [34].

In the next sections it is focused more on electrical and mechanical properties of graphene which makes it a good candidate for NEMS application.

1.2.1. Electrical Properties

In the honeycomb structure of graphene there are two carbon atoms in one unit cell where each carbon atom sits in two triangular lattices with inversion symmetry between them. Such hexagonal arrangement of carbon atoms provides an unusual energy dispersion relation at the Fermi energy of graphene [35]. The carbon sublattices and energy band structure of graphene obtained by simple tight binding model is depicted in Fig. 1.2.

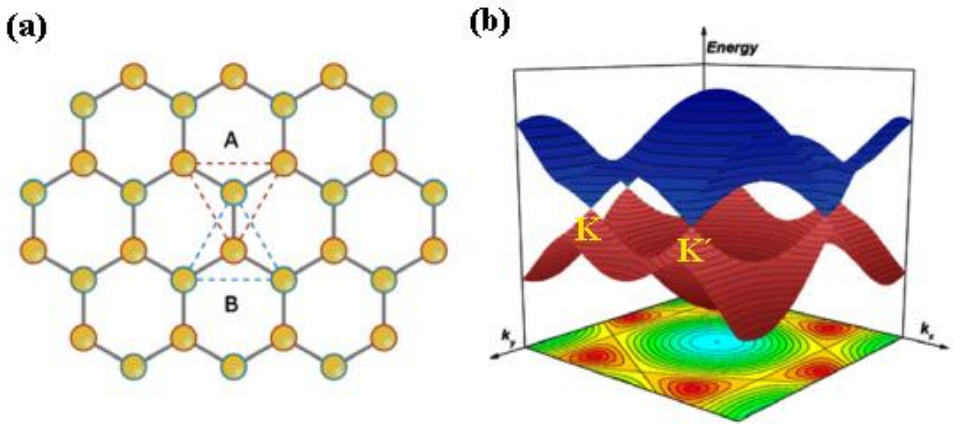

Figure 1.2 – (a) Carbon sublattices (A & B) in crystal structure of graphene, (b) band structure of graphene. K and K´ are the points where the conductance and valence band touch each other [8].

There are several features that make graphene's electronic properties unique and different from other condensed matter systems:

The first feature is graphene's electronic spectrum which resembles the Dirac spectrum for fermions [36, 37]. In the honeycomb lattice of graphene the electrons lose their effective mass which results in quasiparticles that cannot be described by Schrodinger equation and should be

described by Dirac-like equation [38]. It is the consequence of graphene's crystal structure which consists of two equivalent carbon sublattices A and B which are depicted in Fig. 1.2.

Quantum-mechanical hopping between these sublattices leads to the formation of two energy bands: the valence band ($E < 0$) and the conduction band ($E > 0$). These bands touch each other at six points at the corners of the Brillouin zone called Dirac points of which two sets of points are in-equivalent [35]. These two points in reciprocal lattice - called Dirac points (K and K´) - represent different linear superposition of Bloch wave functions in two real sublattices [39]. As a result, quasiparticles in graphene exhibit a linear dispersion relation as if they were massless relativistic particles. In this case the Fermi velocity $v_F \approx c/300$ plays the role of the speed of light [12]. Because of the linear spectrum, it is expected that quasiparticles in graphene behave differently from those in conventional metals and semiconductors where the energy spectrum can be approximated by a parabolic dispersion relation.

The second feature is that graphene exhibits an astonishing electronic quality. It is predicted that because of its perfect crystal structure, the electrons can travel submicrometer distances without scattering [40]. This fact leads to the high mobility of graphene which is in the range of 10,000 $cm^2/V.s$ and is practically independent of temperature [12]. Such mobility which is an order of magnitude higher compared to modern Silicon transistors, ensures ballistic transport on submicron distances [41]. The mobility at room temperature is limited by impurities of the graphene surface, which means that it can be improved significantly, perhaps up to 60,000 $cm^2/V.s$. Some of the methods that are reported to improve the mobility are suspending the graphene flake or current annealing [39].

The third feature is the possibility of fabrication of nano-dimensions graphene devices [42, 43] which enables the miniaturization of the electronic and mechanical devices.

Such different behavior electronic properties that are mentioned here make it a good candidate for future electronic applications [41].

1.2.2. Mechanical Properties

Like most of the carbon allotropes graphene also shows robust mechanical properties. However its mechanical behavior has been much less investigated compared to its electrical properties. Usually there are some problems in measuring the intrinsic mechanical properties of

graphene. These problems include for example uncertainty in sample geometry and stress concentration at clamping points [44].

In some researches the mechanical properties of graphene are measured by dynamic methods such as resonating suspended graphene in vacuum [45, 46]. Dynamic methods lead to highly accurate measurement of the resonant frequencies, but it is not easy and direct method to determine the absolute amplitude of motion.

In contrast nanoindentation with atomic force microscopy (AFM) is used to probe the stress-strain response of graphene [44]. This method allows the accurate and direct measurements of the dimension, displacement and applied force for the suspended graphene flakes. Subsequently, it is possible to measure the spring constant of the flake more precisely. In this way graphene is suspended over open holes forming a nanodrum or in the form of nano-ribbon. Investigation of the behavior of graphene in the form of nanodrums have some advantages: the sample geometry can be precisely defined, the 2D structure is less sensitive to the presence of a single defect and the flake is clamped around the entire hole circumference, in contrast to two points in the case of nano-ribbons.

By static deflection measurements (AFM), the stiffness of the order of 300–400 N/m, and a breaking strength around. 42 N/m, is reported as the intrinsic strength of a defect-free sheet [44, 47]. The Young's modulus of graphene is estimated to be approximately 0.5–1.0 TPa which is very close to the accepted value for bulk graphite [48]. These values combined with the relative low-cost of production of graphene makes this material ideal candidate for mechanical applications. A single sheet graphene bears tremendous potential as the ultimately thin material for NEMS applications such as pressure sensors and resonators.

1.3. Piezoresistivity

Piezoresistivity is the change in the electrical resistance of a material when a strain is applied. The piezoresistors are often used in combination of MEMs or NEMS. The change in the resistance with the elongation was first discovered for iron in 1856 by William Thomson [49]. After that it was confirmed for polycrystalline and amorphous materials by other researchers [50, 51]. The first commercial piezoresistive silicon strain gauge and pressure sensors started to appear in the late 1950's [52]. In 1957 Mason and Thurston reported silicon strain gauges for measuring displacement, force and torque [53]. These sensors were the first commercial devices

requiring three-dimensional micromachining. As a result, this technology was a singularly important precursor to the MEMS technology [54]. The field benefited also from the developments in silicon processing and modeling for the integrated circuits (IC) industry. The technological advances in the mentioned fields improved the sensitivity, resolution, bandwidth and miniaturization of piezoresistive devices [55]. Currently, Piezoresistors are widely used in NEMS as cantilever, pressure, force and mass sensors [56].

The electrical resistance (R) of the material depends on its dimension and resistivity (ρ) [56]:

$$R = \frac{\rho l}{a} \tag{1.3.1}$$

In this equation l and α are the length and cross sectional area respectively. When a stress or a strain is applied to a material, it will lead to changes in the resistance because of changing its resistivity or physical dimensions. The former case is the dominant factor in semiconductors. When a semiconductor is strained the distance between its atoms will change. This will lead to the change in the band gap and the shape of the valance and conduction band. In continue this change will affect the mobility and resistance of the material. So the piezoresistivity of semiconductors is significant. In the latter case the change in the resistance is caused by the changes of the aspect ratio. The change in the dimensions is mostly the dominant factor in the metals.

As a result, when the stress or strain is applied the change in the resistance (ΔR) is due to both the geometric effects (1+2ν) (ν is the Poison's ratio) and the fractional changes in resistivity (Δρ/ρ) of the material with the induced stress or strain [57]:

$$\frac{\Delta R}{R} = (1 + 2\nu)\varepsilon + \frac{\Delta \rho}{\rho} \tag{1.3.2}$$

usually the piezoresistivity effect is determined by a Gauge factor (GF) which is defined as:

$$GF = \frac{\Delta R/R}{\epsilon} \tag{1.3.3}$$

typical values of GF of approximately 1.4 to 2.0 can be achieved by the change in the geometry. The effect of the resistivity change provides a small GF for metal (in the range of 0.3). However for some materials such as silicon and germanium in certain directions the resistivity term is 50-100 times larger than the geometric term. In general the piezoresistive GF reported for metals, semiconductors and organometallic materials are in the range of 2-12, 5-175 and 100-500 respectively [58].

1.3.1. Piezoresistive Materials

The first piezoresistive materials that are used vastly in commercial and research piezoresistive MEMS or NEMS devices are silicon and germanium or their alloys. The reason is their high GF compared to the metallic elements and easy fabrications. It is possible to get a GF up to 175 and 102 from P type silicon and germanium respectively. But the problem is that their GF is not as high as organometalic materials. Besides they are not suitable for chemical harsh and high temperature environments [59]. On the other hand organometalic materials are not stable enough to be used in the micromechanical strain sensors [4]. Consequently, with the advances in materials science and device fabrications newer materials are tested to be used in this field. In this section some of these piezoresistive materials are explained in summary:

- *Diamond:* Comparing to silicon, diamond has also some advanced properties which makes it a good candidates for NEMS in the elevated temperature and harsh environments [60-63]. Such properties include physical hardness, higher Young modulus, higher tensile yield strength, greater chemical inertness, lower coefficient of friction and higher thermal conductivity. The piezoresistive GF for single crystal and poly-crystalline diamond is reported to be around 2000-3836 and 10-100 respectively. However these values depend greatly on doping concentration and temperature [64].

- *Carbon Nanotubes (CNT):* Mechanically nanotubes are among the strongest and most resilient materials in nature. The Young modulus of CNT is on the order of TPa and its tensile strength is two order of magnitude higher than steel [65]. Electronically, CNTs can be metallic, semiconducting or small-gap semiconducting [66]. Yong et al. have measured for the first time the GF of the pristine CNTs that were synthesized by hot filament CVD [4]. In this research a GF of 65 is achieved for CNT thin films at room temperature. According to them such a large GF cannot be ascribed to the changes in the band gap as the band gap of CNT is small. They propose that more likely the defects of the CNT play an important role in such a big GF. For example the deformation of some defects may shorten the length of the ballistic transport along a CNT. Grow et al. have also reported the observation of piezoresistive effect in single tube CNT adhered to a deformable silicon nitride membrane by Van der Waals interactions. In this case it is assumed that the nanotube experiences the same strain as the membrane. In this experience the conductivity of the pressurized CNT decreases which they attribute it to the changes in the band

gap. In such conditions the GF of the semiconducting and small gap semiconducting CNTs are around 400 and 850 respectively [5] whereas the maximum achievable GF in silicon is 200 [67].

Considering, the unique physical and chemical properties of the CNT and its piezoresistive effect it can be said that carbon nanotube has a potential application in nanoelectronics.

- *Graphene:* besides the promising electrical and mechanical properties of graphene which is explained in Sec. 1.2, the interplay between these two is a new field of research. The reason is the rather flexible electronic character of graphene under the stress. But since today the piezoresistivity of graphene is reported only theoretically. Poetschke et al. have used a semiempirical method to model the electrical response of graphene nano ribbons according to an applied force [3]. In their work the band structure of armchair-edge (AGNR) and zigzag-edge (ZGNR) nanoribbons are compared in the relaxed and strained condition (Fig. 1.3). As it is shown in Fig. 1.3.a the AGNR shows initially a semimetallic behavior. After applying a uniaxial force the electronic structure of the system is affected significantly and it depicts a semiconducting behavior. It is also clearly seen that all the degeneracies at the Z points are lifted under strain (Fig. 1.3.b). Differently from AGNR geometry, as it is seen in Fig. 1.3 c and d the band structure of ZGNR does not change significantly under the strain. As a result, ZGNRs can be qualified as unsuitable candidates for the electromechanical nanodevices.

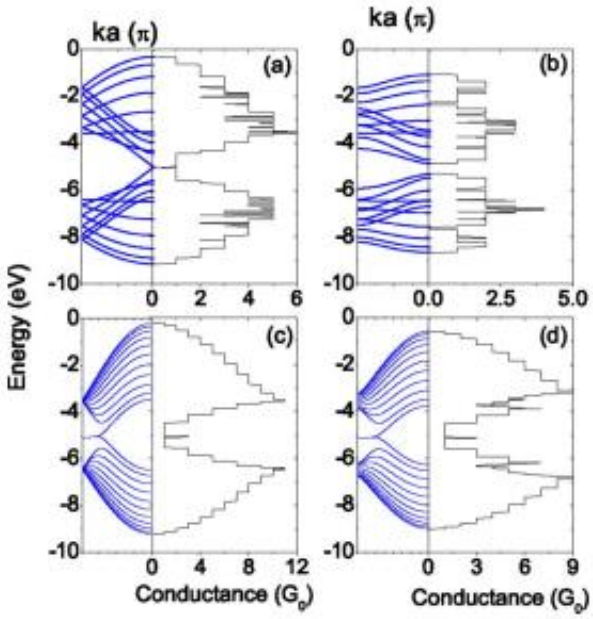

Figure 1.3- The band structure and conductance for (a), (c) relaxed and (b), (d) strained AGNR (N=11) and ZGNR (N=10) [3].

In another research, Medvedyeva et al. have investigated the piezoconductivity of graphene suspended on top of a gate theoretically [6]. They have considered an AFM tip for deformation of the suspended flake. According to them the deformation of the graphene affects the conductivity by inducing change in the band structure as well as by changing the electron density over the flake. The latter is proved to be the dominant factor for small residual stress. But in the case of strong deformation (i.e. using an AFM tip) changing the band structure is more significant. In general still more experimental and theoretical investigations on graphene are necessary to make it ready for Piezoresistors applications.

Chapter 2

Nanomechanics

Nanomechanics deal with the study and application of the fundamental mechanical properties of the physical systems at nanoscale. In this chapter the concepts of continuum mechanics is used to study nanoscale mechanical devices.

2.1. Forces and Stresses

The stress notion quantifies the surface or body forces act to a body in equilibrium. The body forces such as the gravity act inside the body, whereas the surface forces act on its bounding surface. The stresses are those forces distributed over an infinitesimal unit area cut out of a body in a certain direction, or over an infinitesimal unit area on the bounding surface [68].

By assuming a body subjected to an external load as shown in Fig. 2.1, the influence of the load on an interior point can be studied.

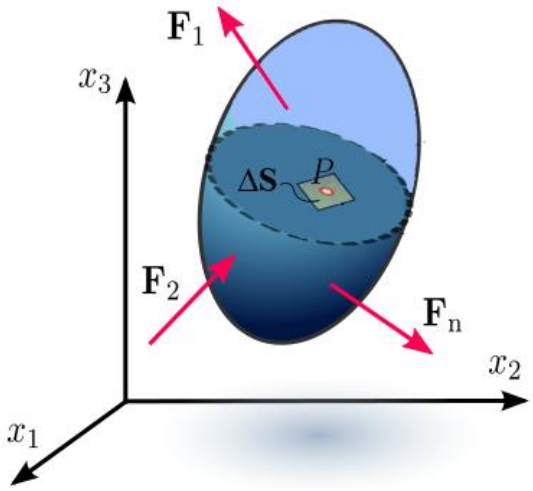

Figure 2.1 – A continuum body subjected to some external forces[1]

the definition of the stress tensor σ in the undeformed state is:

$$\sigma = \lim_{\Delta A \to 0} \frac{\Delta F}{\Delta A} = \frac{dF}{dA} \qquad (2.1.1)$$

here, ΔF is the internal force activated on the area ΔA, from the applied external load. The internal force $dF = \sigma.dA$, can also be considered as a force acting on an inclined surface dA_i of an infinitesimal body (Fig. 2.1). In such case, the infinitesimal force dF can be written in this form:

$$d\boldsymbol{F} = \boldsymbol{\sigma}.dA = \boldsymbol{\sigma_i}.i_i.dA = \boldsymbol{\sigma_i}.dA_i = \boldsymbol{\sigma_{ij}}.i_j.dA_i \qquad (2.1.2)$$

[1]Ref: http://en.wikipedia.org/wiki/Stress_(mechanics)

in Equ. 2.1.2, σ_i's denotes the components of the stress vector σ acting on the inclined surface *dA*. These are the resultant stress vectors on the surface dA_i projected from *dA* on each side of the three planes constructed on the Cartesian coordinate axes. And as it is shown in Fig. 2.2 the σ_{ij}'s are the components of the stress on these projected areas.

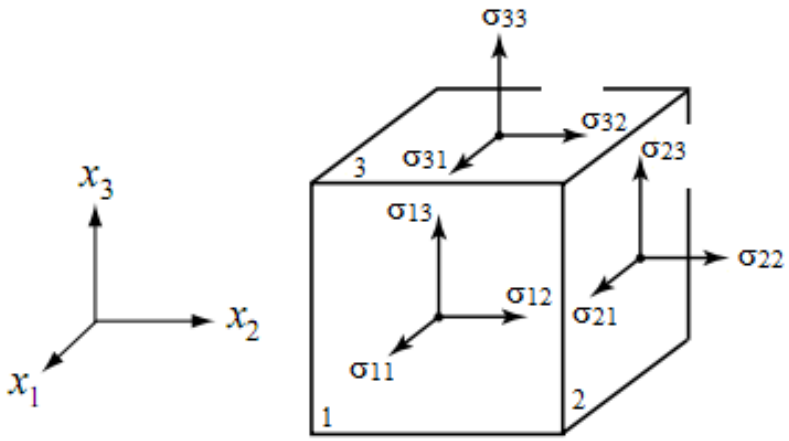

Figure 2.2- Elements σ_{ij} of the stress tensor σ [69]

From Equ. 2.1.2, we can derive the stress tensor σ_{ij}, which is a symmetric matrix as follows [69]:

$$\sigma_{ij} = \begin{bmatrix} \sigma_{11} & \sigma_{12} & \sigma_{13} \\ \sigma_{21} & \sigma_{22} & \sigma_{23} \\ \sigma_{31} & \sigma_{32} & \sigma_{33} \end{bmatrix} \tag{2.1.3}$$

and from the stress tensor, the stress vector is derived for each face:

i.e. for face 1: $t_1 = T_{11}\hat{X}_1 + T_{12}\hat{X}_2 + T_{13}\hat{X}_3$

2.2. Balance Laws

2.2.1. Balance Of Linear Momentum

The definition of the linear momentum *P* within a volumetric unit *dV* is the velocity vector (ν) summed over the incremental mass:

$$P = \int_M \nu dm = \int_V \nu \rho dV \tag{2.1.4}$$

where m and ρ are the mass and density respectively. The rate of the change of the linear momentum is then defined as the sum of the forces including body forces and stress at the surface, working on the element:

$$\frac{dP}{dt} = \frac{d}{dt}\int_V v\rho dV = \int_V F dV + \int_{\delta V} \sigma(n) dA \qquad (2.1.5)$$

in which σ (n) is the stress vector normal to the surface:

$$\sigma(n) = \sigma_i n_i = \sigma_{ij} i_j n_i \qquad (2.1.6)$$

here each n_i is the component of a vector normal to the surface. Using the Green-Gauss theorem the integral over the boundary (δV) of the element can be converted into an integral over the volume [2]:

$$\int_{\delta V} \sigma dA = \int_V \partial\sigma_{ij} / \partial x_i \hat{X}_i dV \qquad (2.1.7)$$

from Eq. (2.1.5) and (2.1.7) we obtain:

$$\int_V (\sigma ijij + F - \rho\dot{v}) dV = 0 \qquad (2.1.8)$$

So far no specification has been applied about the shape or size of the element, so Eq. 2.1.8 should be valid for all arbitrary volumes. Then it yields to Cauchy's first law of motion or simply equation of motion:

$$\rho\dot{v} = \frac{\partial\sigma_{ij}}{\partial x_i} + F_j \qquad (2.1.9)$$

2.2.2. Balance Of Angular Momentum

The time rate of angular momentum is given by:

$$\frac{d}{dt}\int_V r \times \rho v dV = \int_V r \times F dV + \int_A r \times \sigma(n) dA \qquad (2.1.10)$$

with similar analysis for the angular momentum Cauchy's second law of motion can be derived:

$$\sigma_{ij} = \sigma_{ji} \qquad (2.1.11)$$

by applying the boundary conditions to the mentioned equations the stress distribution can be calculated for a given applied force profile [2].

2.3. Strain Tensor

The motion of a rigid object, subjected to various external forces, is described by the position of the object's center of mass, and the orientation of the object with respect to a fixed set of coordinate axes. Therefore, rigid body mechanics is only an approximation to the actual motion of the solid, as it ignores all the internal motions when an object is acted upon by external forces; these external forces will cause the deformation, or strain of the object.

Consider a rigid body with a fixed point *P* at position r inside the body (Fig. 2.3), when the body is strained, point *P* will shift to a different point *P´* at position *r´* with respect to the center of mass of the object. Here it is assumed that the object does not move or rotate. Hence a coordinate system that is fixed to the center of mass of the body can be used, and it is assumed that the resulting non-inertial effects (due to the object's acceleration and rotation) are small or slow enough that they can be ignored.

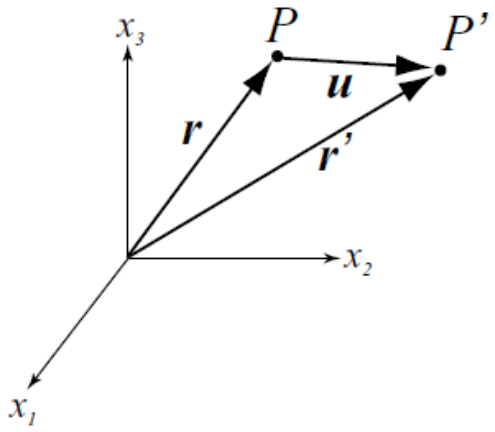

Figure 2.3 - Displacement of the point *P* at position *r* to the point *P´* at position *r´* under relative displacement *u*.

the strain-induced displacement of *P´* with respect to *P* is the vector $u = r´ - r$**.** The displacement vector *u* varies with position *r* within the body, and is time-dependent, so it can be written as $u(r, t)$. Now, if one considers two points in a small distance, *P* at position *r* and *Q* at position $r+\Delta r$ (Fig. 2.4). Under the strain *P* displaces to *P´*, located at $r+u(r)$, and *Q* displaces to *Q´*, located at $r+\Delta r+u(r+\Delta r)$.

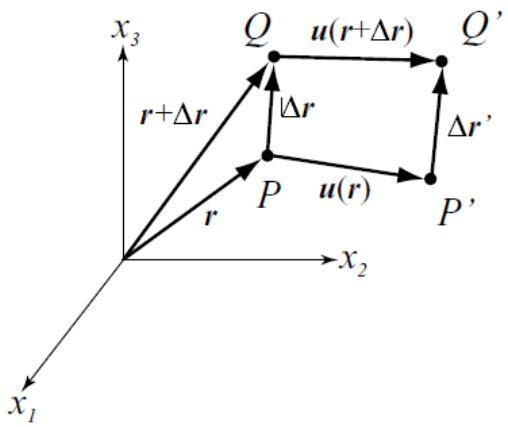

Figure 2.4 - Points *P* and *Q*, initially separated by Δr, shift under the induced strain to *P´* and *Q´* separated by Δr´.

the position of *Q* with respect to *P* is *Δr*, and the position of *Q´* relative to *P´* is $\Delta r' = \Delta r + u(r+\Delta r) - u(r)$. Therefore the strain-induced relative displacement of *Q* with respect to *P* is introduced as:

$$\Delta u = u(r+\Delta r) - u(r) \tag{2.3.1}$$

as a result, the position of *Q´* with respect to *P´* is:

$$\Delta r' = \Delta r + \Delta u \tag{2.3.2}$$

if the *Q* and *P* would be infinitesimally close, *Δr* would be a differential vector. In this case each component u_i of the displacement *u(r+Δr)* can be expanded in a vector Taylor series about the point *r*:

$$u_i(r+\Delta r) = u_i(r) + \sum_{j=1}^{3} \frac{\partial u_i}{\partial x_j} \Delta r_j + ... \tag{2.3.3}$$

ignoring the higher order terms Δu_i would be:

$$\Delta u_i = \sum_{j=1}^{3} \frac{\partial u_i}{\partial x_j} \Delta r_j \tag{2.3.4}$$

the strain-induced relative displacement of any two points is calculated by integrating these partial derivatives $(\partial u_i / \partial x_i)$ in the appropriate way; these derivatives are assembled in a tensor (*D*) which is the basis of the definition for the strain tensor:

$$\varepsilon = \nabla u \tag{2.3.5}$$

it is possible to rewrite *D* as a symmetric and antisymmetric part [70]:

$$\varepsilon = S + \Omega \tag{2.3.6}$$

$$s = \frac{1}{2}(\nabla u + (\nabla u)^T) \tag{2.3.7}$$

$$\Omega = \frac{1}{2}(\nabla u - (\nabla u)^T) \tag{2.3.8}$$

then the symmetric and antisymmetric parts are defined as strain tensor and rotation tensor respectively. Writing in component form, the strain tensor is:

$$s_{ij} = \frac{1}{2}(\frac{\partial u_i}{\partial x_j} + \frac{\partial u_j}{\partial x_i}) \tag{2.3.9}$$

and in tabular form:

$$s = \begin{pmatrix} \frac{\partial u_1}{\partial x_1} & \frac{1}{2}(\frac{\partial u_1}{\partial x_2} + \frac{\partial u_2}{\partial x_1}) & \frac{1}{2}(\frac{\partial u_1}{\partial x_3} + \frac{\partial u_3}{\partial x_1}) \\ \frac{1}{2}(\frac{\partial u_1}{\partial x_2} + \frac{\partial u_2}{\partial x_1}) & \frac{\partial u_2}{\partial x_2} & \frac{1}{2}(\frac{\partial u_2}{\partial x_3} + \frac{\partial u_3}{\partial x_2}) \\ \frac{1}{2}(\frac{\partial u_1}{\partial x_3} + \frac{\partial u_3}{\partial x_1}) & \frac{1}{2}(\frac{\partial u_2}{\partial x_3} + \frac{\partial u_3}{\partial x_2}) & \frac{\partial u_3}{\partial x_3} \end{pmatrix} \tag{2.3.10}$$

like the stress tensor, the strain tensor is also symmetric.

2.4. Elasticity And Compliance Tensors

The forces acting on the material are described by stress tensor whereas the strain tensor gives information about the deformation of the material. As they are both symmetric it is possible to write them in a 6 component vector format. For small deformations the stress and strain are linearly related to each other by the elasticity tensor:

$$\begin{bmatrix} \sigma_{xx} \\ \sigma_{yy} \\ \sigma_{zz} \\ \sigma_{xz} \\ \sigma_{yz} \\ \sigma_{xy} \end{bmatrix} = \begin{bmatrix} E_{xxxx} & E_{xxyy} & E_{xxzz} & E_{xxxz} & E_{xxyz} & E_{xxxy} \\ E_{xxyy} & E_{yyyy} & E_{yyzz} & E_{yyxz} & E_{yyyz} & E_{yyyx} \\ E_{xxzz} & E_{yyzz} & E_{zzzz} & E_{zzzx} & E_{zzzy} & E_{zzxy} \\ E_{xxxz} & E_{yyxz} & E_{zzzx} & E_{xzzx} & E_{xzzy} & E_{yxxz} \\ E_{xxyz} & E_{yyyz} & E_{zzzy} & E_{xzzy} & E_{yxxz} & E_{xyyz} \\ E_{xxxy} & E_{yyyx} & E_{zzxy} & E_{yxxz} & E_{xyyz} & E_{xyyx} \end{bmatrix} \begin{bmatrix} S_{xx} \\ S_{yy} \\ S_{zz} \\ S_{xz} \\ S_{yz} \\ S_{xy} \end{bmatrix} \tag{2.4.1}$$

or in short format:

$$\sigma_{ij} = E_{ijkl}\, S_{kl} \tag{2.4.2}$$

The elasticity tensor is a forth ranked tensor with 81 distinct elements. However the symmetry of the stress and strain tensor is imposed to the elasticity tensor. As a result, the number of independent elements reduces to 36. Further reductions can be made by using the symmetries of

the materials. By considering an isotropic material with full rotational symmetry the number of independent values is reduced only to two: the Young module *E* and the Poisson's ratio *v*.

The inverse of the elasticity tensor is called the compliance tensor which expresses the strain in terms of stress [2, 69]. Equ. 2.4.3 and 2..4.4 depict elasticity and compliance tensors for an isotropic material:

$$[C] = \begin{bmatrix} 1/E & -\nu/E & -\nu/E & 0 & 0 & 0 \\ -\nu/E & 1/E & -\nu/E & 0 & 0 & 0 \\ -\nu/E & -\nu/E & 1/E & 0 & 0 & 0 \\ 0 & 0 & 0 & 1/G & 0 & 0 \\ 0 & 0 & 0 & 0 & 1/G & 0 \\ 0 & 0 & 0 & 0 & 0 & 1/G \end{bmatrix} \tag{2.4.3}$$

$$[E] = \frac{1}{(1+\nu)(1-2\nu^2)} \begin{bmatrix} E(1-\nu) & E\nu & E\nu & 0 & 0 & 0 \\ E\nu & E(1-\nu) & E\nu & 0 & 0 & 0 \\ E\nu & E\nu & E(1-\nu) & 0 & 0 & 0 \\ 0 & 0 & 0 & G & 0 & 0 \\ 0 & 0 & 0 & 0 & G & 0 \\ 0 & 0 & 0 & 0 & 0 & G \end{bmatrix} \tag{2.4.3}$$

For non-isotropic materials, the Young modules and Poisson's ratio are defined considering the direction of the applied stress: $E_i = 1/C_{iiii}$ and $\nu_{ij} = -C_{iijj}/C_{iiii}$ ($i \neq j$) [71].

2.5. Bending Rigidity, Tension and Equation Of Motion For Plates

Based on Ref. [68], the equations of motion are derived from the energy needed to deform the material. This energy depends on the strain and it should be invariant under coordinate transformations if the deformation is small:

$$U = \int_V U' dV \qquad \text{in which} \qquad U' = \frac{1}{2} E_{ijkl} S_{ij} S_{kl} \tag{2.5.1}$$

when the material is considered to be isotropic U' becomes [72]:

$$U' = \frac{1}{2} \frac{E}{1+\nu} \left(S_{ij}^2 + \frac{\nu}{1-2\nu} S_{kk}^2 \right) \tag{2.5.2}$$

As this research is about graphene, at this section our discussion is focused on a material in a thin plate format in order to make the calculations simpler. Assume a thin plate under longitudinal tension T, which is bent. In this condition its total potential energy consists of:

$$U = U_B + U_T + U_F \tag{2.5.3}$$

in which U_B is energy needed to bend the plate:

$$U_B = \frac{Eh^3}{24(1-\nu^2)} \iint \left[\left(\frac{\partial^2 u}{\partial x^2} + \frac{\partial^2 u}{\partial y^2} \right)^2 + 2(1-\nu) \left(\left(\frac{\partial^2 u}{\partial x \partial y} \right)^2 - \frac{\partial^2 u}{\partial x^2} \frac{\partial^2 u}{\partial y^2} \right) \right] dxdy \tag{2.5.4}$$

and U_T is the energy of stretching which is the result of the restoring force caused by the tension:

$$U_T = \frac{1}{2} \iint S_{\alpha\beta}\, T_{\alpha\beta}\, dxdy \text{ where } T_{\alpha\beta} = h\bar{\sigma}_{\alpha\beta} \tag{2.5.5}$$

and U_F is the effect of an external force F in z-direction:

$$U_F = -\iint F u dxdy \tag{2.5.6}$$

by considering the variation of the total potential energy for an arbitrary variation of the displacement ($u \rightarrow u+\delta u$), the equation of motion is derived for the vertical deflection of the plate:

$$\rho h \frac{\partial^2 u}{\partial t^2} + \left(D\nabla^4 - \frac{\partial}{\partial x_\alpha} \mathrm{T}_{\alpha\beta} \frac{\partial}{\partial x_\beta} \right) u(x,y) = F(x,y) \tag{2.5.7}$$

here ρ is the mass density and D is the bending rigidity. D expresses the amount of energy which is needed to bend a unit area of the plate and is calculated from:

$$D = \frac{E_{in}\, h^3}{12(1-\nu^2)} \tag{2.5.8}$$

here E_{in} is the in-plane Young's module. In case of the few layer graphene the bending rigidity is calculated by [73-75]:

$$D = \frac{E_{in}\, h^3}{12(1-\nu^2)} \frac{N-1}{N} \tag{2.5.9}$$

in which N is the number of layers. According to this equation the bending rigidity is vanished for a single layer of graphene. But molecular dynamics simulations have shown that single layer of graphene still has a finite bending rigidity [73, 75]. By considering the modification of the bending rigidity, it is possible to describe the mechanical behavior of graphene by continuum mechanics [76, 77].

2.6. Graphene Nanodrums

In this section the theoretical and experimental studies on mechanical behavior of a few layer graphene suspended on top of a hole (so-called nanodrum) are reviewed. In one of these researches Poot et al. have modeled the deformation of a graphene nanodrum which is caused by a point force [2]. The condition of their modeling is depicted in Fig. 2.5.

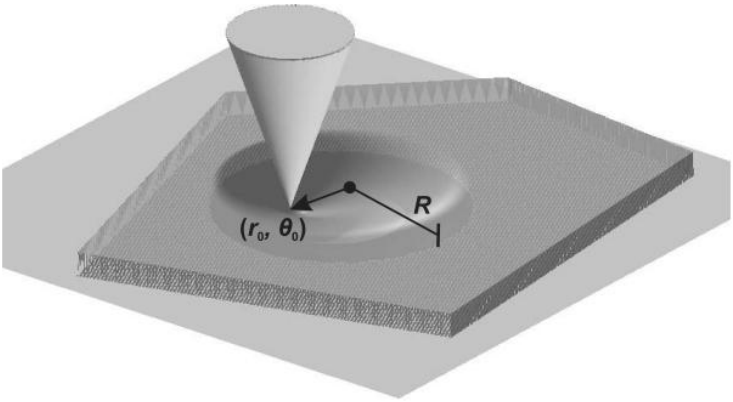

Figure 2.5 – Schematic view of few layer graphene suspended on top of a hole with radius R forming a nanodrum. An AFM tip is used to apply a force on point (r_0, Θ_0) and deform the nanodrum.

In the case of deforming a nanodrum, there are three variants that contribute in the restoring force which opposes the applied force:

- The bending rigidity of the flake *D*
- A tension that may be present in the flake *T*

by replacing these terms in Eq. 2.5.7, they have calculated equation of motion for nanodrum:

$$\left(D\nabla^4 - \frac{\partial}{\partial \mathrm{x}_\alpha}\mathrm{T}_{\alpha\beta}\frac{\partial}{\partial \mathrm{x}_\beta}\right)u(x,y{:}\,x_0,y_0) = F_{tip}\,\delta(x-x_0,y-y_0) \qquad (2.6.1)$$

where $T_{\alpha\beta} = \int_0^h \sigma_{\alpha\beta}\,dz$ and the ∇-operator and partial derivatives $\frac{\partial}{\partial \mathrm{x}_\mathrm{i}}$ are working in the xy-plane only, and the z-dependence is absorbed in the bending rigidity.

Eq. 2.6.1 is solved by applying the boundary conditions. Assuming the isotropic tension and ignoring the external pressure the deflection profile for the small deflections compared to the thickness of the flake is given in polar coordinates by:

$$(D\nabla^4 - \mathrm{T}\nabla^2)u(r,\theta{:}\,r_0,\theta_0) = \frac{F_{tip}}{r}\,\delta(r-r_0,\theta-\theta_0) \qquad (2.6.2)$$

The calculated deflection profile at the point where the force is applied is illustrated in Fig. 2.6.a. According to their modeling by moving the tip away from the center of the nanodrum the deflection of the flake is reduced. It means that the local compliance decreases. Since the tension is isotropic and the flake is suspended on top of a circular hole the compliance is independent of Θ_0 (Fig. 2.5). In this situation the radial of the compliance reveals all the information. This profile is shown in Fig. 2.6.b for different values of the tension. From the picture it is clearly seen that the tension is a significant factor in nanoscale devices. The profile becomes sharper at

the edge of the hole for a large tension and rounded when the tension is smaller. For more information on non isotropic tension refer to Ref. 2.

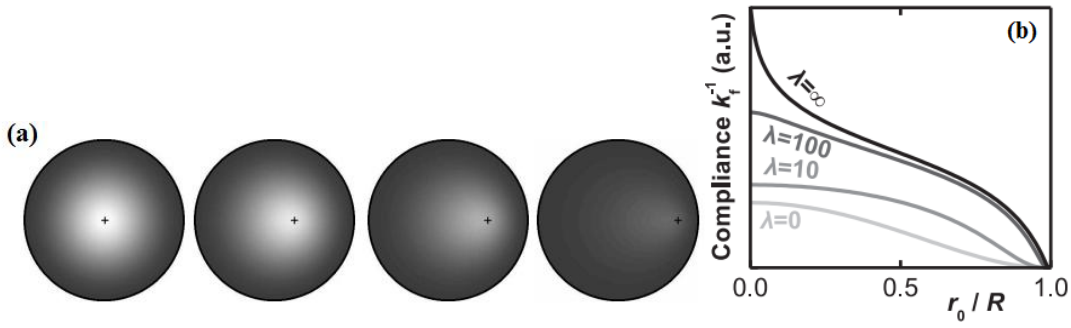

Figure 2.6 – (a) Colormaps of the calculated deflection profiles (Eq. 2.34) of a nanodrum with vanishing tension. The force is applied at the location of the cross and the color scale is identical in all four panels: white corresponds to a large deflection and dark gray to no deflection, (b) the calculated radial compliance profile for different values of the tension, with $\lambda^2 = TR^2/D$ [2].

Poot et al. have also measured the elastic properties of graphene nanodrums by applying a force with atomic force microscope (AFM) under ambient conditions. They have derived the map of the local compliance by application of the force-volume technique which is explained in chapter 4. This map is depicted in Fig. 2.7.

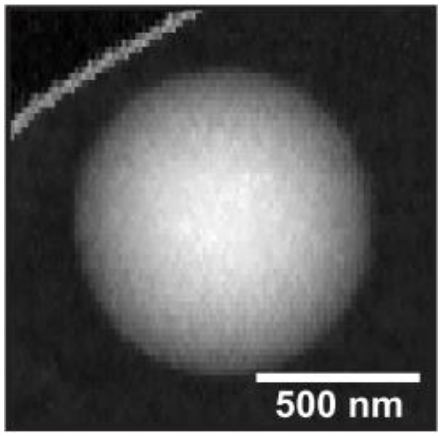

Figure 2.7 – Color map of the compliance of a flake with h = 23nm, extracted from a force-volume measurements (64 by 64 force-distance curves). The range of the compliance is from 0 (black) to $9.7.10^{-3}$ m/N (white) [2].

In order to compare the results of the experiment with the theory and find the bending rigidity and the tension of the flakes, the compliance profiles calculated with the continuum model for the induced deflection are fitted to the experimental data. From Fig. 2.8 it is clearly seen that the good fits are obtained with this model.

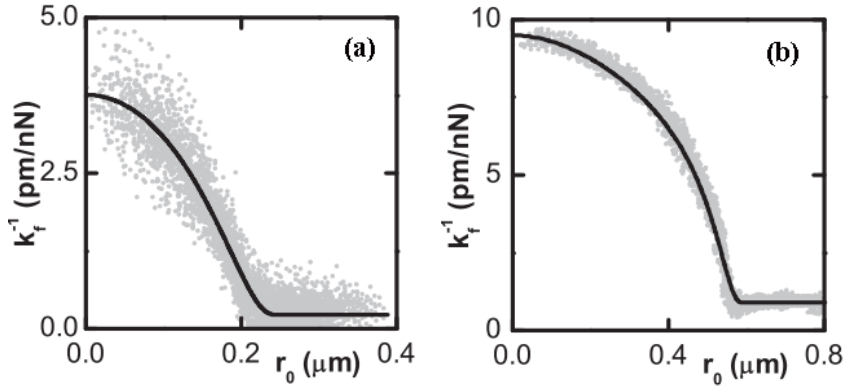

Figure 2.8 – (a) The measured radial profile of the compliance (symbols) of a 15nm thick flake and the fit by the model (Equ. 2.6.2) (solid line). (b) The radial profile of the data shown in Fig. 2.7 [2]

The fitting of the data in Fig. 2.8.a reveals that for this flake the bending rigidity is the dominant factor of the compliance. It is seen that the profile is rounded at the edges. On the other hand the profile in Fig. 2.8.b is for a flake which is fitted with a large tension. That is the reason of the sharp edges of the profile.

According to the results of these experiments the bending rigidity does not depend on the hole size and it is an intrinsic property of the flake [2]. The tension is also uniform throughout the flake. It means that probably the tension is induced during the deposition process [27].

In summary, AFM measurements of the compliance profile of a suspended flake can reveal important information about its mechanical properties. Merging the results achieved from this technique with electrical properties of graphene can yield to the information about its piezoresistivity which is the goal of this research.

Chapter 3

Sample Fabrication

3.1. Fabrication Of Graphene Nanodrums

In this research graphene is studied in the shape of nanodrums. A nanodrum which is illustrated schematically in Fig. 3.1 is formed by suspending a thin layer of membrane on top of a hole. In our case the membrane is a few-layer graphene sheet which is suspended on top of a hole.

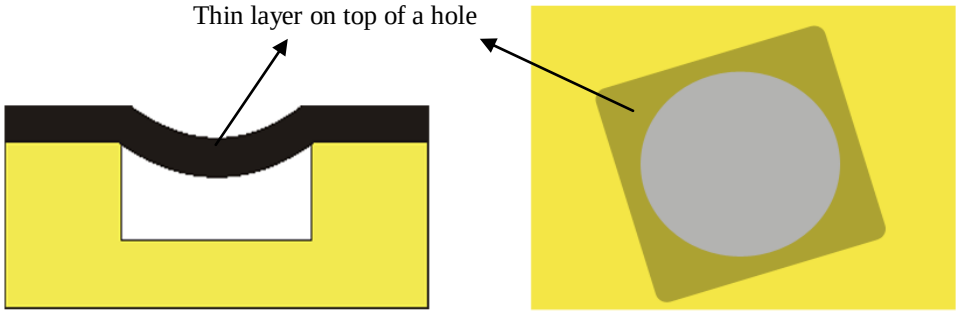

Figure 3.1- Schematic illustration of a thin film suspended on top of a hole, forming a nanodrum, (Right) top view (Left) cross section view.

In researches done so far on graphene [24, 27] it is reported that the few-layer graphene is visible in an optical microscope, when placed on top of an oxidized silicon substrate with a special thickness of silicon oxide [24, 27, 78 and 79]. A small difference in the silicon oxide thickness can make single layer of graphene invisible. Hence, silicon with 285nm silicon oxide on top was selected as the substrate in this research [80].

In order to make the graphene nanodrums, first of all the 7μm by 7μm substrate is divided to cells and rows by fabricating gold markers and cell numbers on it. These cells and markers are used for addressing the parts of the substrate which the graphene flakes are deposited. They are also used for the alignment of the sample for later steps like electron-beam lithography (E-beam). Then the holes are formed on the substrate by etching. Each cell contains 486 holes with the diameter about 1μm. After that the graphene is deposited to the surface by mechanical exfoliation to form the drums. At the last step the gold contacts are fabricated around the flakes that cover a hole completely. In the next section all the steps of the sample preparation are described in detail.

3.1.1. Fabrication Of The Markers And Cell Numbers

To fabricate the drums, first of all the substrate is cleaned by sonicating for 2 minutes in subsequently nitric acid, water and IPA[1]. Afterwards, as it is shown schematically in Fig. 3.2, the surface is coated with two layers of PMMA[2] 495 A4 (5000 rpm, baked at 150°C for 1 min) and one layer of PMMA 950 A3 (6000 rpm, baked at 150°C for 1 min) as the resist. Then a pattern of the markers and cell numbers are written by E-beam. In the next step, the resist is developed by MIBK[3]/IPA with ratio of 1:3 for 2 minutes and then IPA for 1 minute. This step removes the parts of the resist that are exposed to the E-beam; as a result, the pattern is transformed on the resist (Fig. 3.2).

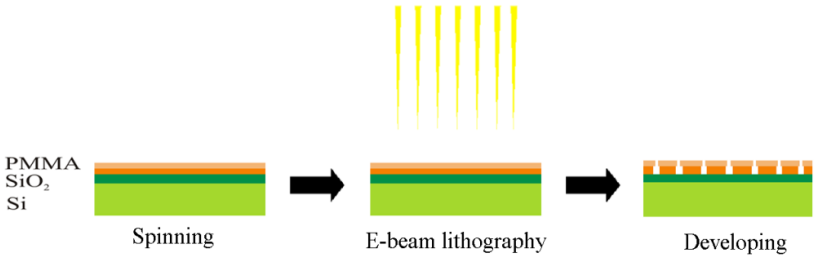

Figure 3.2- Schematic process of E-beam lithography and developing for formation of the markers, the pattern is written on the resist by E-beam lithography and is transferred to the resist after its developing

Subsequently, 5nm of chromium and 50nm of gold are evaporated on the substrate (Fig. 3.3). In this case the gold covers the surface where there is no resist and transfers the pattern to the surface, the rest parts are removed by lifting off the resist. For lift off, the sample is put in warm acetone (55°C) for around 3 hours and then is cleaned with IPA.

Figure 3.3- Schematic illustration of evaporation of gold to transfer the pattern from resist to the substrate and the lift-off process of the resist

[1] Isopropyl alcohol
[2] Polymethyl-methacrylate
[3] Methyl isobutyl ketone

One of the designed cells of the substrate with its markers and cell numbers is shown in Fig. 3.4. In this cell the numbers show the number of the row and column of the cell respectively and the squares are the markers which are used in E-beam lithography.

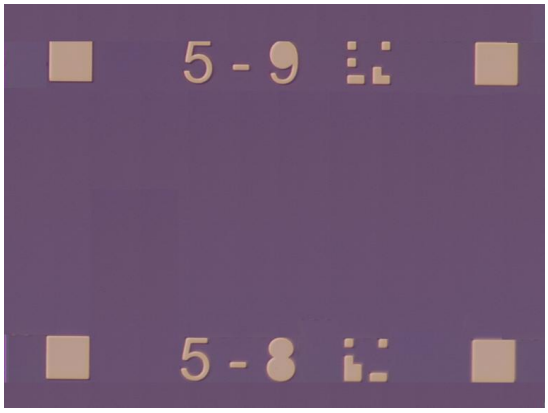

Figure 3.4- One of the designed cells fabricated on the substrate, which contains cell numbers and markers that are used for further designs

3.1.2. Fabrication Of The Holes

After creating the markers and cell numbers, the holes are formed on the substrate. Fig. 3.5 depicts its steps schematically. At first, the surface is coated by two layers of PMMA 950 A3 (6000 rpm, baked at 150°C for 1 min) and the pattern of the holes is written by E-beam. Afterward the resist is developed with the same method as before (Sec. 3.1.1) and the holes are etched in BHF[1] for 100 seconds. The rate of etching for BHF is 80nm/min, so the approximate depth of the holes is around 130 nm. After etching of the holes, the resist is lifted off in warm acetone like what it is mentioned above.

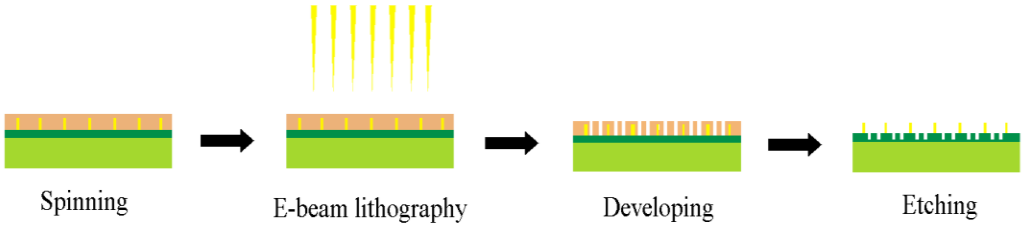

Figure 3.5- Schematic illustration of E-beam lithography and etching for forming of the holes

[1] Buffered hydrofluoric acid

Fig. 3.6 illustrates the holes that are formed on the substrate.

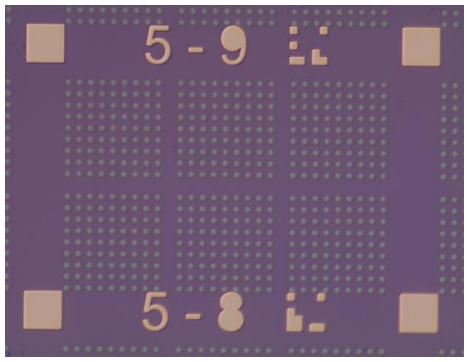

Figure 3.6- Holes that are formed on the substrate

3.1.3. Graphene Deposition

Before depositing the graphene, first the substrate is cleaned and prepared. To find the optimum method of cleaning and preparation, three different methods are used, which are:

A. The substrate is sonicated for 2 minutes subsequently in nitric acid, water and IPA. Afterward, it is dried with nitrogen, then is coated with HMDS [1] and is left to get dry in the air. HMDS is used to make the surface hydrophobic [81]. When the HMDS gets dried the sample is rinsed again with IPA and is put on the hot plate at 110°C for 5 minutes to be sure that no solvent has remained on the surface. Three samples are cleaned by this method, but after graphene deposition rarely a few layer graphene is achieved.

B. The substrate is cleaned first with Piranha (H_2SO_4/H_2O_2 with the ratio of 1:3), and then with IPA. After that the sample is put on the hot plate at 110°C for 5 minutes to dry completely. One sample is cleaned by this method, but after graphene deposition no few layer graphene is achieved.

C. The substrate is sonicated for 2 minutes subsequently in nitric acid, water and IPA. Then after drying it with nitrogen, it is cleaned with oxygen plasma for 30 seconds. Three samples are prepared by this method and it seems that plasma oxidation increased the adhesion of the flakes to the substrate, because after graphene deposition more than 20 few-layer graphene flakes are found on the substrate.

consequently method (C) is used as the optimum cleaning method for making the samples.

[1] Hexa methyl di silazane

To prepare the graphene flakes, the graphite (NGS graphite) is stuck to blue NITTO tape (SPV 224P) and the graphene flakes are achieved by the mechanical exfoliation. After the cleaning, the tape is stuck and pushed softly to the substrate and the graphene flakes stick to the surface. Fig. 3.7 depicts the graphene flakes achieved after the graphene deposition.

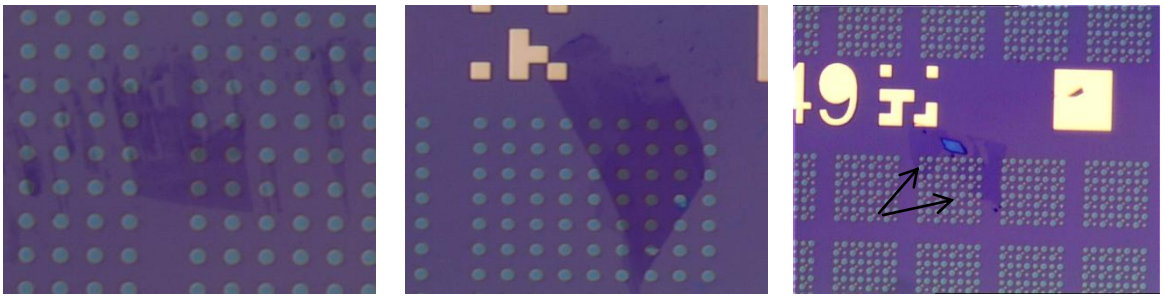

Figure 3.7- Graphene flakes covering the holes after the graphene deposition to the substrate

For the case of nanodrums, the deposition of few layer graphene with exfoliation of graphite at the end does not guaranty to have a flake completely covering a hole. As a result, a recently invented method called wedging [82] is also tested on one sample. In this method the graphene flake is floated on water and after transferring on top of the target spot of the substrate, the water level is lowered until the flake touches the substrate.

But the results show that at the end all the flakes are broken. The reason is the remaining water on the holes that after evaporating the surface tension applied on the flake will suck the flake down to the bottom of the hole and break it. Consequently, it is understood that wedging cannot be used for fabrication of the drums with the holes which their bottoms are closed; and in order to get good flakes by this method some modifications should be applied in our fabrication process. If the holes are designed in such a way that their bottom would be open then the wedging method is applicable because the water is removed from the end of the hole and does not stuck into the hole.

3.1.4. Fabrication Of The Electrodes

In the next step, an optical microscope is used to find the thin flakes with less than 15 layers of graphene which cover a hole completely. The number of layers of the flakes is first estimated according to their optical contrast [83]. Afterward the thickness of the flakes is measured more precisely by AFM. When the best flakes are selected, the surface is coated again by resist which

consists of two layers of PMMA 495 A4 (5000 rpm, baked at 150°C for 1 min) and one layer of PMMA 950 A3 (6000 rpm, baked at 150°C for 1 min). Then the pattern of the gold contacts is designed around the flakes on top the holes, and is written by E-beam. After that the resist is developed with the same method that is mentioned above. Later 5nm of chromium and 50nm of gold are evaporated to create the contacts around the nanodrums followed by lift off in warm acetone. Fig. 3.8 shows one of the nanodrums with the gold electrodes around it. In this step the sample cannot be dried normally with nitrogen because the tension of liquid which remains on the holes from the previous steps breaks the flakes. Consequently after lift off the sample is transferred to IPA very fast and a critical point dryer (CPD) was used to make the samples dry.

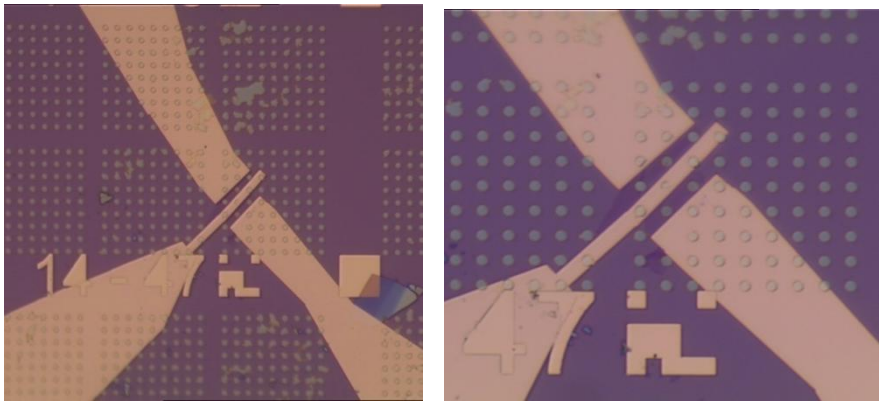

Figure 3.8- Gold electrodes around a graphene nanodrum

When the devices are formed, they need to be connected to the electrical setting which is used in this research. As a result the substrate is pasted to a circuit board which is explained in detail in the next section.

3.2. Circuit Board

After preparing the devices their conductivity is checked. Usually each substrate contains around 10-12 devices, but not all of them are necessarily conductive. In order to check them a probe station and a beeper are used which are explained here:

The probe station is a device which utilizes some manipulators that allow the precise positioning of thin needles on the contacts of the devices and apply a voltage on them.

The beeper, which is a device for measuring the resistance between two leads, is connected to the source and drain of the device through the probe station. It applies a voltage to the leads and

emits a tone when there is a resistance between the leads and shows the amount of the resistance. It also shows if the circuit is open.

As a result the sample is placed on the probe station and its resistance is measured by applying 10 mv to the source and drain of the device by the beeper. If it is not open or the resistivity is not very high (not more than 50 kΩ), the device is conductive and is used for further measurement.

After that the sample is glued on top of a circuit board using silver paste and the devices are bonded to it by aluminum bonding wires. Fig. 3.9 illustrates one of the samples connected to a circuit board. The circuit board which is soldered to the connectors is used to place the sample on AFM and connect it to the electrical equipments which are mentioned in the next section. In this case, it is possible to apply a bias or gate voltage to each device and measure the connectivity of the device or gate current.

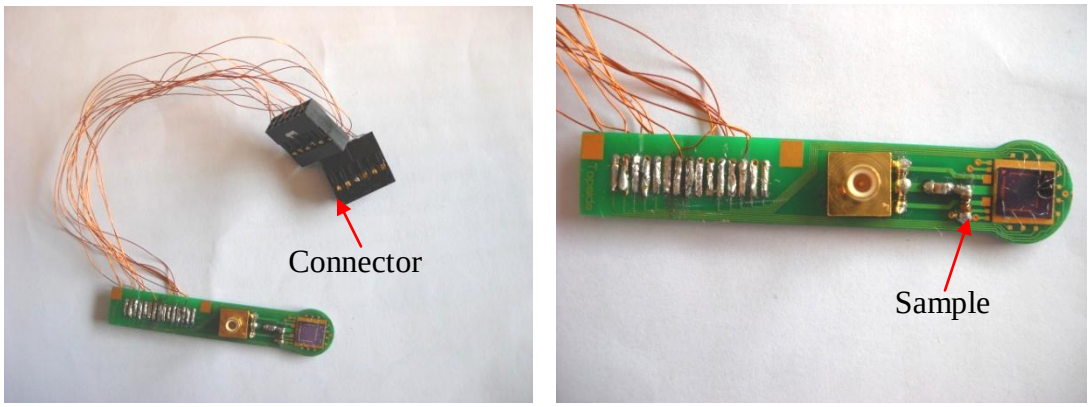

Figure 3.9- The substrate is glued on a circuit board and then the devices are bonded to the substrate and the substrate is soldered to the connectors in order to be able to connect to the electrical setups

In the next chapter the instruments and tools that are used for measurements of the devices are explained in more detail.

Chapter 4

Measurements

As it is explained in Sec. 1.3, the general concept of measuring the piezoresistivity is applying a force and meanwhile measuring the conductivity of the samples. In this research, the force is applied with an atomic force microscopy (AFM) under ambient conditions. The AFM which has been used is extended with additional electrical setup to enable applying a voltage to the device and measuring its conductivity. In this chapter first the basic principles about AFM and the applied force are discussed, and later the electrical setup is explained briefly.

4.1. Atomic Force Microscopy

Atomic force microscopy is commonly used for atomic and nano-scale measurement of various properties, including surface topography and interfacial forces [84, 85]. The principle of AFM is based on a cantilever deflection which is measured by a laser beam deflection sensor. As it is shown schematically in Fig. 4.1.a, it consists of a reflective cantilever with a sharp tip with which scans the surface. While the tip scans the surface, the cantilever is bent up or down from its equilibrium position, in response to the potential forces between the tip and the sample (Fig. 4.1.b). For example, when the height of the surface increases, the force between the tip and the surface also increases as a result of the reduction of the distance between the tip and the surface. Consequently, the cantilever deflects upward. Its deflection is detected by a laser beam that reflects off the cantilever onto a mirror and finally to a four segment photodiode. When the cantilever is in its free equilibrium position (not deflected), the laser is reflected onto the center of the photodiode. As a result of the cantilever deflection, the laser is reflected onto a different part of the photodiode; the photodiode then senses the displacement of the laser beam and sends an electronic signal to the data processor. Then the data processor calculates height of the sample surface by comparison between the photodiode generated signal and a setpoint value which is related to the equilibrium position of the tip. Then the feedback system controls vertical z position of the cantilever using the photodiode signal and keeps its deflection at the setpoint value by moving the sample up and down[1].

[1] In some AFMs the tip moves instead of the sample

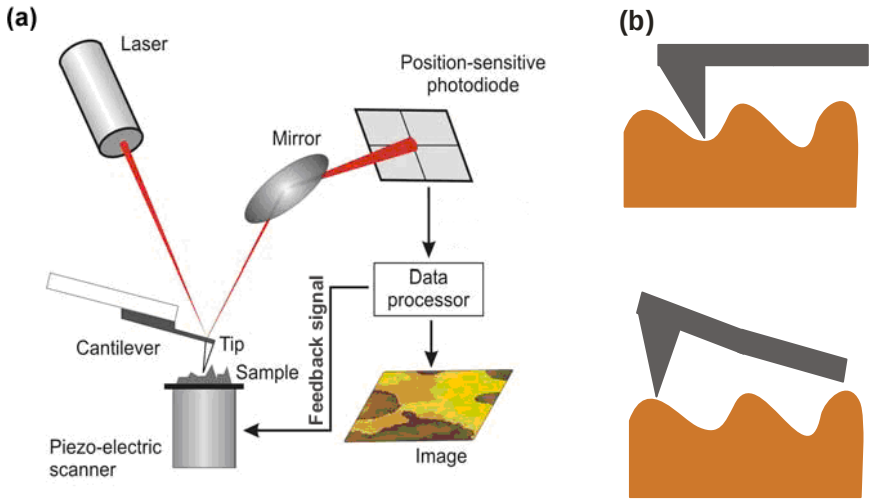

Figure 4.1- (a) Schematic illustration of AFM (taken and modified from Ref. 84), (b) Tip deflection according to the surface roughness

The sample can move relative to the probing tip by a cylindrical piezoelectric tube in x, y and z directions. By scanning the sample and digitizing the deflection of the cantilever as a function of the x and y position AFM images are created.

The complete AFM system that has been used for the experiments in this research is shown in Fig. 4.2. An AFM system consists of two main components: the atomic force microscope and the controlling hardware.

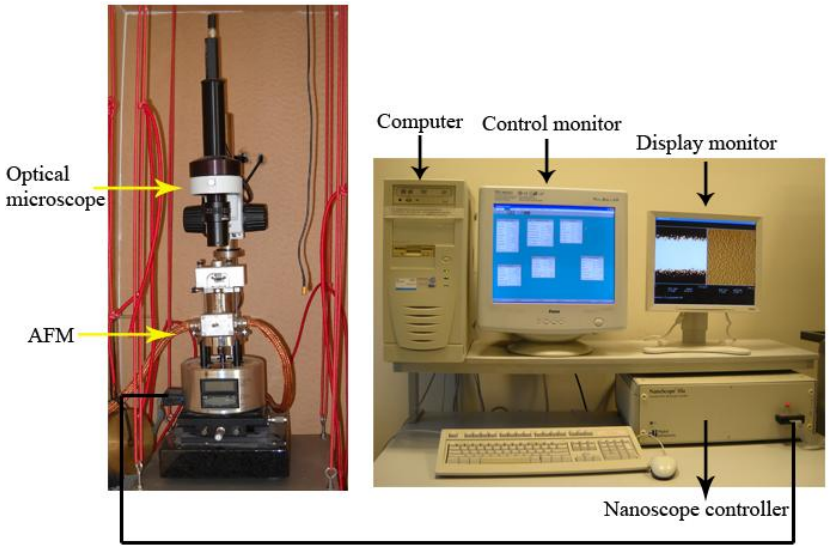

Figure 4.2- (Left) Atomic force microscopy, and (Right) the hardware that are used to control AFM (Multimode SPM with NanoScope IIIa controler)

The main parts of the atomic force microscope are shown in more detail in Fig. 4.3. They include the detection system and the scanner. The detection system which is on top consists of the tip and sample holder, the mirror and the photodiode. The scanner contains the piezoelectric tube which moves the sample and is connected to the base. Base contains some electrical setup and is the connector between the AFM and its hardware. Usually the AFM is connected to an optical microscope in order to adjust the tip on the area that needs to be scanned.

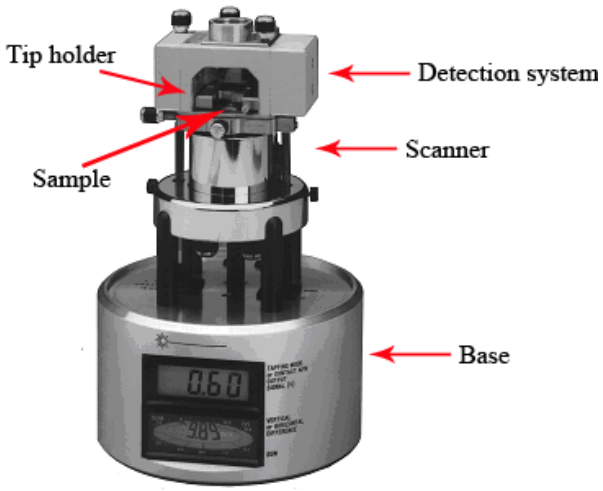

Figure 4.3- Structure of AFM [86]

As it is shown in Fig. 4.2 the AFM hardware includes a nanoscope controller, a computer, a control monitor and a display monitor. Nanoscope controller is the heart of the electrical setup of AFM. All the analysis of the input and output signals, like signals generated by the photodiode, feedback loop and voltages applied to piezo, are done in this module and sent to or taken from the AFM. The computer and the control monitor are the interface between the user and the nanoscope controller. The user can control the scanning condition and also access the output data through the computer by the nanoscope controller software. Display monitor also lets the user to see the results of AFM during and after the scanning.

4.1.1. Operating Modes Of AFM

Considering the distance between the tip and the sample, three basic types of scanning with AFM exist. If the tip-sample separation would be small (in the order of Å) the tip is in contact with the surface. In this mode which is called 'contact mode' or 'static mode', the ionic repulsion

forces allow the surface topography to be traced with high atomic resolution. However this mode can be destructive for soft samples according to the small distance between the tip and the surface and the combination of the lateral forces and high normal forces which may lead to scraping between the tip and the sample [86].

In non-contact mode, the separation is in the range of 10-100 nm. In this mode forces such as van der Waals and electrostatic forces, are sensed and give information about surface topography [87]. This mode is not destructive because of the larger distance from the surface but it has slower scan speed compared to the other modes. The reason of slower scan rate is to avoid the tip getting stuck into the absorbed fluid layer from the environment to the surface [86].

Finally in tapping mode (TM) or dynamic mode the cantilever is driven at a fixed frequency close or equal to its resonance frequency with constant amplitude ranging typically from 20nm to 100nm. During measurement, the vibrating tip touches the sample surface intermittently. As a result of the interface forces the vibration amplitude of the tip changes according to the roughness of the surface. This amplitude is compared to the setpoint amplitude which is maintained by the feedback system and the difference is used as a parameter to track the sample topography. This mode has lower forces on the sample so is less destructive for soft samples [86, 88].

In this research two different techniques of AFM are used in tapping mode, which are: height image and Force-volume technique. The height image is used in order to determine the approximate height of the sample, the dimension of the hole and the condition of the suspended flake. Force-volume technique is used to apply a force and deform the flake. These techniques are described in detail in Sec. 4.3 and 4.4.

4.2. Electrical Setup

It is explained later in Sec. 4.4 that the output of force-volume technique of AFM is only the voltages of the piezo in x, y and z direction and the tip deflection during the measurement of the force-distance curve. These data are used to calculate the applied force on the flake. But for measuring the piezoresistivity, in addition to the data of the AFM voltages, we also need to record the conductivity of the flake while the force is applied at each point. These are necessary to calculate the resistance changes according to the applied force. It is not possible to measure the conductivity by AFM and measuring it separately is not useful, because it cannot be

combined with the data of the applied force for each sample point. As a result an extra electrical setup is added to the AFM to let us apply a voltage to the source-drain and the gate of the device and measure its conductivity. In addition to that, it enables us to measure the voltages of the piezo and the tip deflection from AFM at the same interval that the conductivity of the sample is measured. Consequently, for each sample point, we can have all the necessary data for piezoresistivity at the same time, and merge them in different plots.

During the measurement the sample is a part of a simple circuit which is shown schematically in Fig. 4.4. By this circuit, the bias and gate voltages are applied to the device and the output current is measured. As it is shown, the electrical circuit consists of:

(1) A computer used for introducing the value of the bias voltage that is applied and recording the measured output data. The commands of the user are entered to the setup via the LabVIEW software.
(2) Bias DAC controller which sends the defined value of voltages from the computer to the voltage source via an optically isolated connection.
(3) IV-VI rack which is used as the voltage source and ampere meter. As it is shown in Fig. 4.4, it has different modules which are controlled by DACs. One of the modules is called V-source which is connected to the source and drain of the device through MCX to BNC adaptor (4). In our settings it will apply a voltage in the range of millivolt. Another module is called Iso-V source which is connected to the gate of the device. This one is set to apply a voltage in the range of volt. The third module called I-measure measures the current passes through the device. The current then is passed through an IV converter, with a 10 MΩ conversion factor. The output voltage is measured by another module called dual Iso-out. By this method the current of the device is converted to the voltage in order to be sent to the ADwin-Gold (7).
(4) MCX to BNC adaptor which is used to convert different types of connectors.
(5) AFM matrix box is a board beside AFM, containing the tip and the substrate switches. The Source and the drain of the sample are connected to BNC adaptor through these switches. The gate of the sample is also connected through one of these switches to Iso-V source module of IV-VI rack. During the measurements these switches are on.

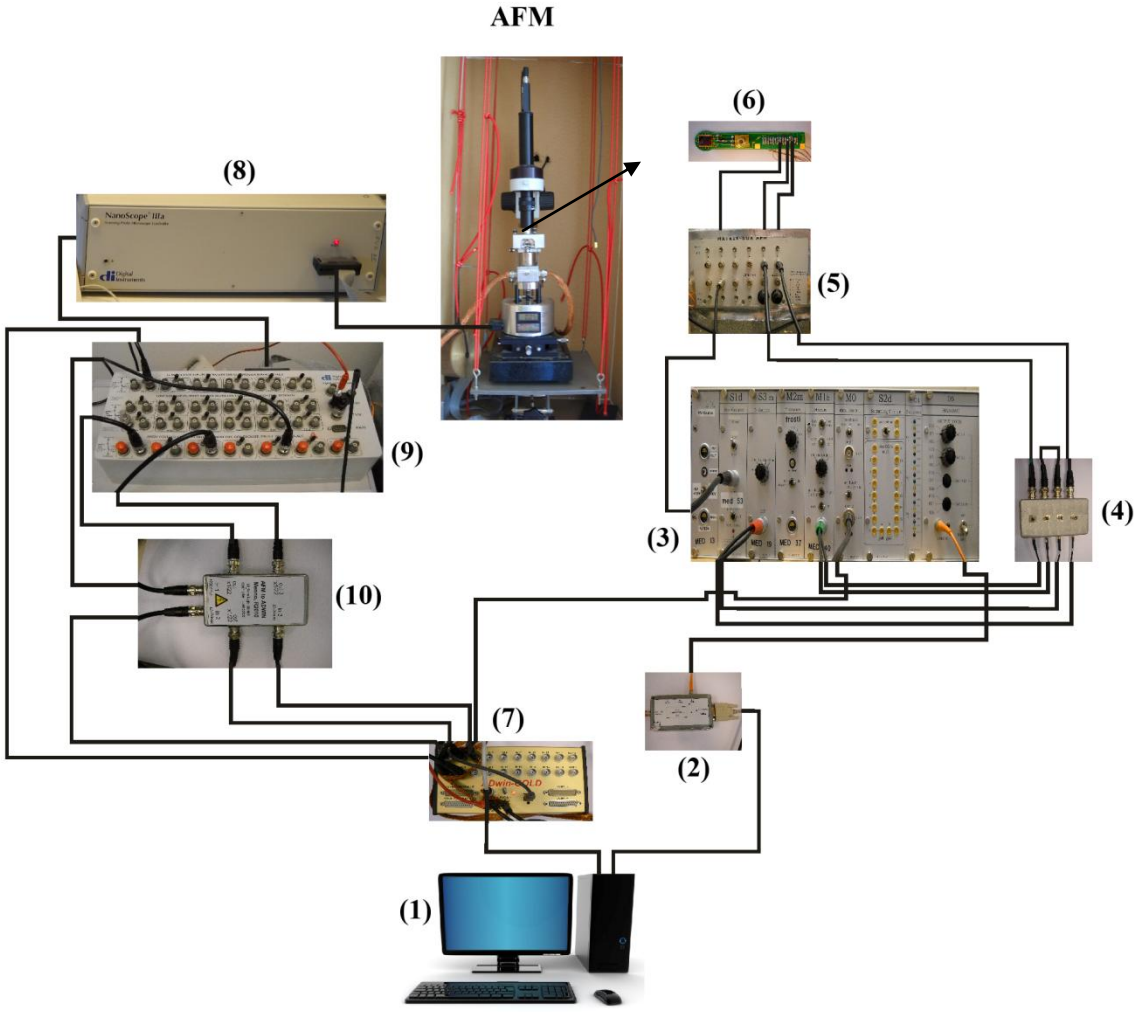

Figure 4.4- Schematic circuit of the electrical setup which enables us to apply a voltage to the flake and measuring its conductivity (right hand module), besides it is possible to measure the voltages of the piezo tube and the tip deflection simultaneously with the conductivity by this setup

(6) This is the circuit board which carries the sample. It has some connectors that are connected to the switches of the matrix box and make the sample a part of the circuit. The sample is placed on the AFM by the circuit board.

(7) Voltages are recorded with the ADwin-Gold USB (called ADwin) systems. This device is connected via a USB to the computer and lets us register the measured voltage by IV-VI rack which is relative to the current of the device. It is also possible to register the measured piezo voltages by signal access controller (9) with ADwin.

(8) The Nanoscope controller which controls the feedback system and the output signals of AFM. It is explained in Sec. 4.1.

(9) Signal access controller which enables the voltages of piezoelectric tubes for x, y, z and the tip deflection to be measured.

(10) AFM to ADwin connector which reduces the output range of the AFM voltage (+220 to -220 V) to the input range of ADwin (+10 to -10 V). it takes the voltages measured by signal access controller as input and multiply it by a factor of 1/22 and sends it to ADwin.

For measurement, by defining a value for the bias and gate voltages on LabVIEW and running the program once by the user, that value enters in the memory of Bias DAC controller and is sent to related modules of IV-VI rack. The IV-VI rack applies the voltages to the source and the gate of the device. Then the AFM is run in the force-volume regime to apply a force (Sec. 4.4) and meanwhile the current passing through the sample is measured and is sent to ADwin.

On the other side, the measured voltages by the AFM signal access controller during the force-volume technique are transferred to ADwin. At the end ADwin sends all of these data to the computer at a specific time distances and they are recorded by time-trace LabVIEW program during the measurement. In our case the time distance between the two samples of ADwin is 1 ms, in other words the voltages of AFM and the current are measured every millisecond.

Consequently, with this setup we can measure the voltages of tip deflection and the piezo in x, y, z direction which let us calculate the force at each point (Sec. 4.4). Meanwhile when the force is applied, we can measure the current of the sample. These data are processed by a program which is made in Matlab in order to get the profiles of the changes in the compliance and resistivity of the graphene flakes. The detail about the program is explained in Sec. 4.3.1 and 4.4.2.

4.3. Height Image

The function of the tapping mode height image is already explained in sec. 4.1. The output of AFM in this mode is an image with a color plot according to height of the surface. Fig.4.5.a depicts the AFM height image of a flake suspended on top of the holes.

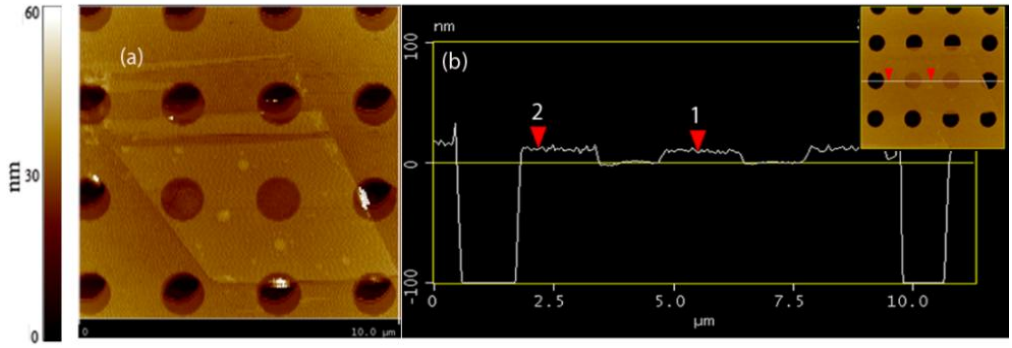

Figure 4.5- (a) AFM Height image of a suspended graphene flake on top of the holes, (b) cross section analysis of the flake to find the height difference between the points of the red markers. The marker # 1 points the flake on top of the substrate and the marker # 2 points the substrate, the inset depicts where the section analysis has been done.

One of the options of the nanoscope's controller software is the section analysis which plots the height difference at the cross section along a line plotted on the surface. This option is used for the height image to measure the thickness of the flake. In Fig 4.5.b the section analyses of the flake along the line which is shown in intersect, is illustrated. By moving the red markers to different points the program shows the height difference between those points. In Fig. 4.5.b marker 1 is on top of the flake and marker 2 is on the substrate. According to the section analysis the approximate difference between the heights of these two points is about 3 nm which shows the thickness of the flake.

For taking the height image one should define for AFM:

- The dimensions of the area that needs to be scanned.
- The velocity with which the tip scans one line of the surface (tip velocity).
- The number of sample points at each line in x and y directions. The voltages of the piezo are measured by AFM at each sample point.

As it was explained before, while taking the height image the voltages of the piezo tubes at x, y and z directions are measured by ADwin. In the next section it is explained that how a program is made in order to reconstruct the height image by using the ADwin data.

4.3.1. Reconstructing The Height Image From The Data Measured By ADwin

In Sec. 4.2 it is explained that in order to investigate the piezoresistivity of the flakes we need to measure the piezo voltages of AFM and the conductivity separately with ADwin. Later we will explain in Sec. 4.4.2 that these data are used to reconstruct the results of the force-distance curve measurements. Making a program that can reconstruct the force-volume results in first step is complicated. Consequently, we first start to make the program for the height image which has less data points and is easier to find logic to reconstruct the image. Later we will apply this logic and improve it to reconstruct the results of the force-volume technique.

In AFM the distance that the tip moves in each direction to scan the sample is (more or less) proportional to the voltages of the piezo in that direction. So the pattern of the changes in the piezo voltage in the x and y direction shows the pattern of the tip motion.

During the height image the voltages applied by the AFM controller to the piezo tube (V_x, V_y and V_z) are measured at every millisecond using ADwin. These data contains the voltages at the coordinates of the sample points and also some electrical noises. Thus the data points of ADwin are more than AFM. The reason is the difference in is the mismatch between the interval that the tip moves from one AFM sample point to the other (depending on the tip velocity and number of sample points) and the interval that the data are measured and recorded with ADwin (1 ms).

As a result a program is made in Matlab to reconstruct the height image by using the voltages measured with ADwin. Before explaining about the program it is necessary to explain in more detail how the tip moves while creating the height image.

Assume that a rectangular area with the dimension of X and Y is scanned (in our case X and Y are equal). For the scanning, the tip moves to one of the corners on bottom or top of the rectangular and starts scanning. Fig. 4.6 shows schematic motion of the tip on x and y direction during scanning. The tip scans the surface line by line by moving in a zigzag fashion in x and y direction. The number of lines is equal to the number of sample points that is defined by the user for AFM in y direction. During the scan of each line AFM records the piezo voltages at some equidistance points. The number of these points is equal to the number of AFM sample points in x direction.

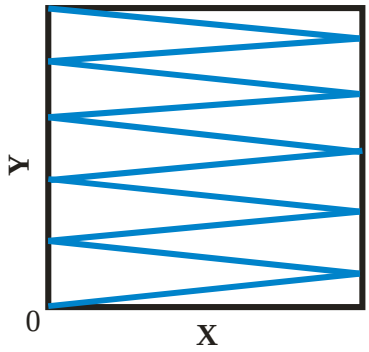

Figure 4.6- Schematic illustration of the tip motion on the surface during scanning the height of the surface

Consequently, these AFM sample points make a grid over the surface. The program reconstructs this grid by finding the approximate voltage of each AFM sample point from the voltages measured by ADwin. Then it fits a surface according to the piezo voltage is z direction over the grid. Here it is explained how the grid is reconstructed.

Fig. 4.7 depicts the changes in voltage of piezo in x direction (V_x) versus time. During the scan of the height of the surface the piezo compresses and extends in x direction repeatedly in order to move the tip forward and backward at each line. The approximate interval of scanning of each line in forward or backward direction is calculated by using length of the line and tip velocity. It is not precise because the extension of the piezo is not completely linear when it extends more than a range. But it can be used to find the time of the first minimum and maximum in V_x. Then the difference between the time of the first minimum and maximum gives a more accurate interval with an uncertainty of approximately 1ms.

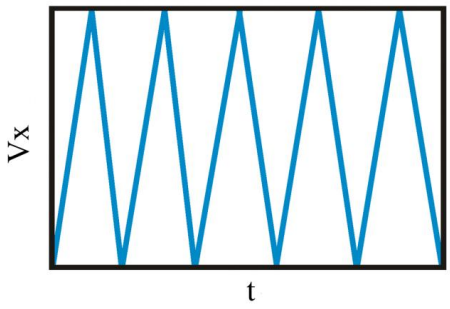

Figure 4.7- Schematic illustration of piezo voltages in x direction vs. time during height image technique of AFM

Furthermore by knowing the interval and the time of the first minimum and maximum, the times of all the minima and maxima values in V_x are found. At this stage, the slope of a line that

fits to all the minima (or maxima) gives an even more accurate interval. To be more precise in our program, a line is fitted first to all the minima and then to all the maxima; the slopes of these lines is equal to the double length of interval because it shows the time that the tip completes scanning one forward and one backward direction. So the most precise interval is achieved by using the average of the slope of those lines.

Fig. 4.8 illustrates an example of the method that is used to derive the coordinate of the tip at each moment from the piezo voltages that are measured by ADwin. By calculating the ratio of the interval which is passed at each moment, it is possible to find the position of the tip on each line.

$$\frac{\Delta V}{V} = constant \times \frac{\Delta L}{L} \qquad (4.3.1.1)$$

Here V and L are the difference between the value of the voltage of the maximum and minimum in the first interval and the length of the scanned line (defined by user) respectively. By using double length of an interval in this method it is also possible to calculate the coordinate of the tip separately for forward and backward direction at each moment. For example, in Fig. 4.8 assume that the line scan starts at t = 60. (This is the time of the first point of the interval when x=0). Then For scanning a line with the length of 1µm if we consider double length of interval as 2 seconds, at the moment when one quarter of the interval is passed (t = 60.5 sec), the tip is in the coordinate of x=0.5µm in the forward direction (Point A). When the tip reaches to half of the interval (t = 61sec), it finishes one forward motion and starts to move backward (Point B). After passing three quarter of interval (t = 60.5), the tip is in x=0.5µm in the backward direction (Point C).

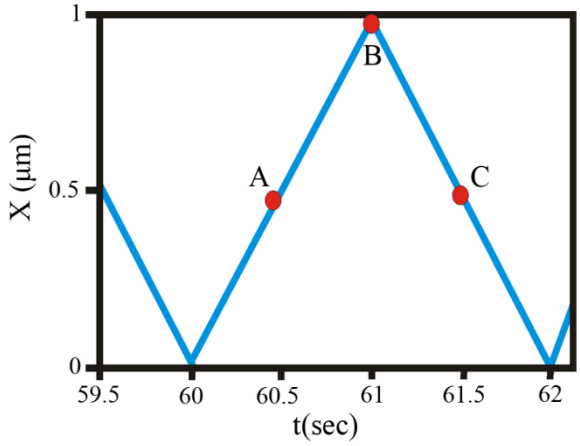

Figure 4.8- Calculating the motion of the tip in x direction from the double length of an interval

The next step after converting V_x to x coordinate of the tip at each moment is to find its y coordinate, which its period is equal to the time of the beginning and ending of the scanning. Usually measuring of the voltages starts by the time-trace program before the tip reaches to the top or bottom corner and starts scanning. The reason is that it is not easy to start measuring exactly at the same time that the tip starts scanning so the time-trace program is run it a few seconds earlier. As a result in the program the extra voltages should be omitted before reconstructing the image. It is done while finding the y coordinate of the tip at each moment.

To find the coordinate of the tip in y direction first the interval in y direction is found. The interval in y direction is equal to the time in which the AFM scans all the lines in forward and backward direction. It means that during this time AFM scans the defined area once. Consequently, if we assume that scanning starts from the bottom, the minimum in y piezo voltage is the first point of the first interval in x piezo voltage; and the maximum of y piezo voltage is the last point of the last interval of x piezo voltage or vice versa (It is vice versa if the tip starts scanning from the top).

Assume that the scanning starts from the bottom, to determine the first point of scanning, the time difference between the minimum of V_y (V_{ymin}) and the first minimum and maximum of V_x are compared respectively. The one that has smaller time difference with V_{ymin} is considered as the first point. In order to find the last point of scanning, at first the length of V_y and interval of V_x are used to find the last maximum and minimum of V_x. Furthermore, the time difference between the maximum of V_y (V_{ymax}) and the last minimum and maximum of V_x are compared, and the one which is closer in time to V_{ymax} is considered as the last point. When the first and the last point of scanning are determined, the interval in y direction is calculated. After that, the y coordinate of the tip at each moment is calculated with the same method which is used for x, by using V_y and the y interval. At the end the voltages of the times before and after the y interval are omitted from the x and y voltages. Once knowing the x and y coordinate the surface is gridded according to the number of sample points in x and y direction.

Furthermore, the coordinate of the piezo in z direction which shows the height of the sample at different points is derived by dividing the z piezo voltage by the z piezo sensitivity. In our AFM scanner the z piezo sensitivity is equal to 12.8 mV/nm. In continue a value of z is interpolated to each point of the grid. The result of this step is a matrix consisting of z value at each point of the grid. The number of sample points in x direction determines the number of the columns of the

matrix and the number of sample points in y direction determines the number of the rows. By creating the matrix, a surface with the form of z = f(x, y) is fitted to the grid. In other words, the program will interpolate a surface at the points of the grid according to the z piezo coordinate.

Fig.4.9 depicts the AFM height image of a graphene flake taken from two different area (a, c) and their reconstructed image from the measured data with ADwin (b, d). Comparing Fig. 4.9.a and b it is seen that they are more or less the same, but with some small differences, i.e. in the shape and the place of the holes. But Fig. 4.9.d is very similar to its AFM image (Fig. 4.9.c). The differences are mostly because of the nonlinearity in the extension of the piezo tube when it extends more than a critical range. This is very small but it makes some shifts in the reconstructed image. As in the program the changes in the piezo voltages are considered to be only linear. This is clearly visible when we compare the accuracy of Fig. 4.9 b with d. In Fig. 4.9.b the length of the scanned area is larger than d, as a result the piezo extends more and the effect of the nonlinear extension appears more. That is why Fig. 4.9.b is less accurate than Fig. 4.9.d comparing to their AFM images. Besides the electrical noises that are inevitable in the ADwin data and other approximations that are made in the program causes some changes in the reconstructed program. But in general it can be concluded that the logic which is used to make this program can further be applied for reconstruction of the results of the force volume technique.

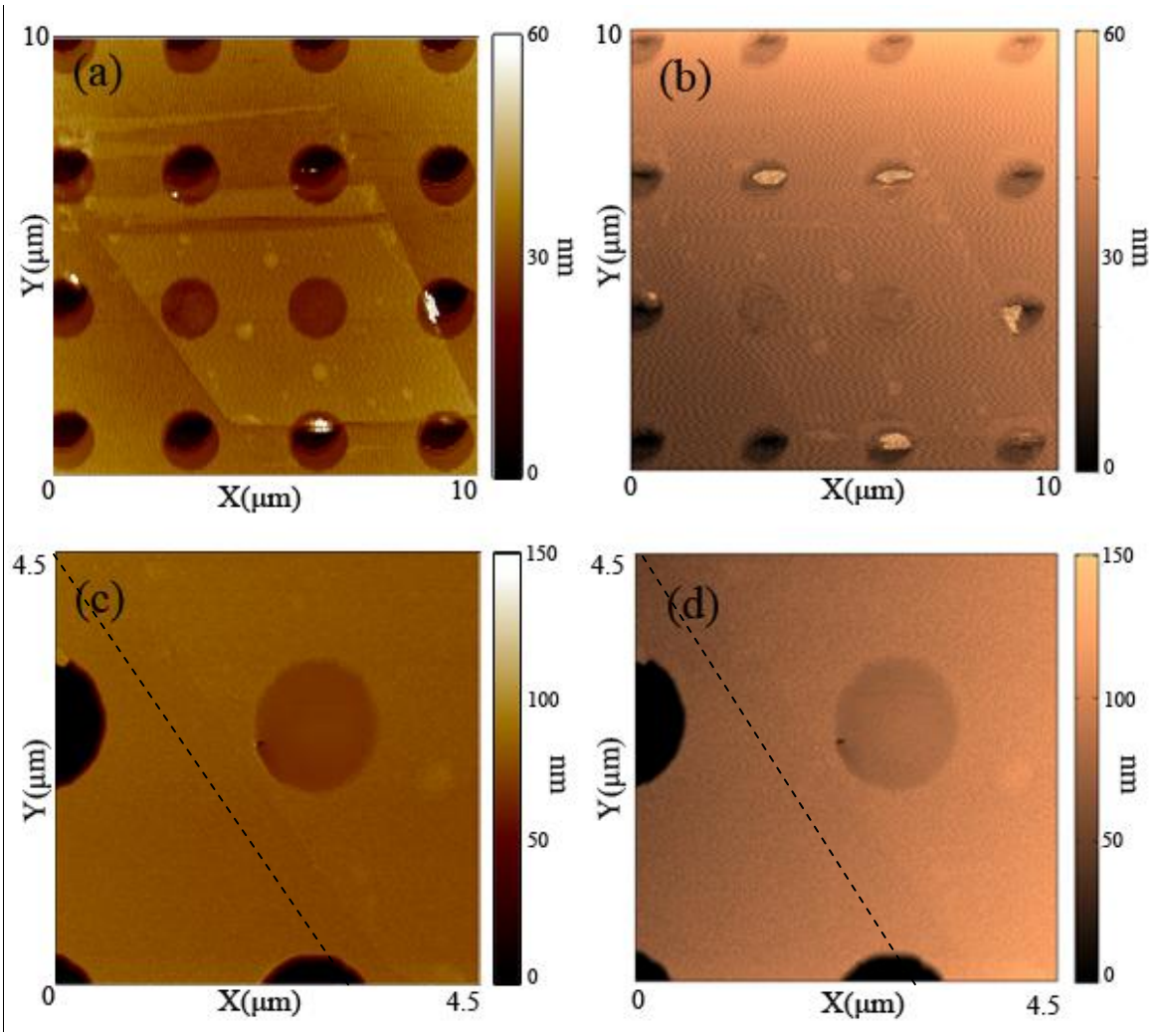

Figure 4.9- Height image of a graphene flake suspended on top of a hole (a, c) image taken by AFM, (b, d) image reconstructed by a program made in Matlab (dashed line shows the boundary of the flake)

Another technique which is used to apply a force on the sample is force-volume technique. In next section, this technique is explained in more details.

4.4. Force-Volume Technique

Force-volume technique is a technique of AFM in which multiple force-distance curves are recorded while scanning the surface in a rectangular grid over the sample [89]. In our research this technique is used to apply a force on the flake in order to deform it and measure its compliance profile. The force distance curve which is depicted in Fig. 4.10.a is used to get some information about the mechanical properties of the material.

In Fig. 4.10.b it is shown that how a force-distance curves is measured. In order to measure the force-distance curve of a point, the tip approaches the surface from a specific distance (Z_{piezo}) until a maximum deflection of the cantilever (Z_{tip}) occurs. Afterward the tip is retracted from the surface and goes back to the same height as before approaching.

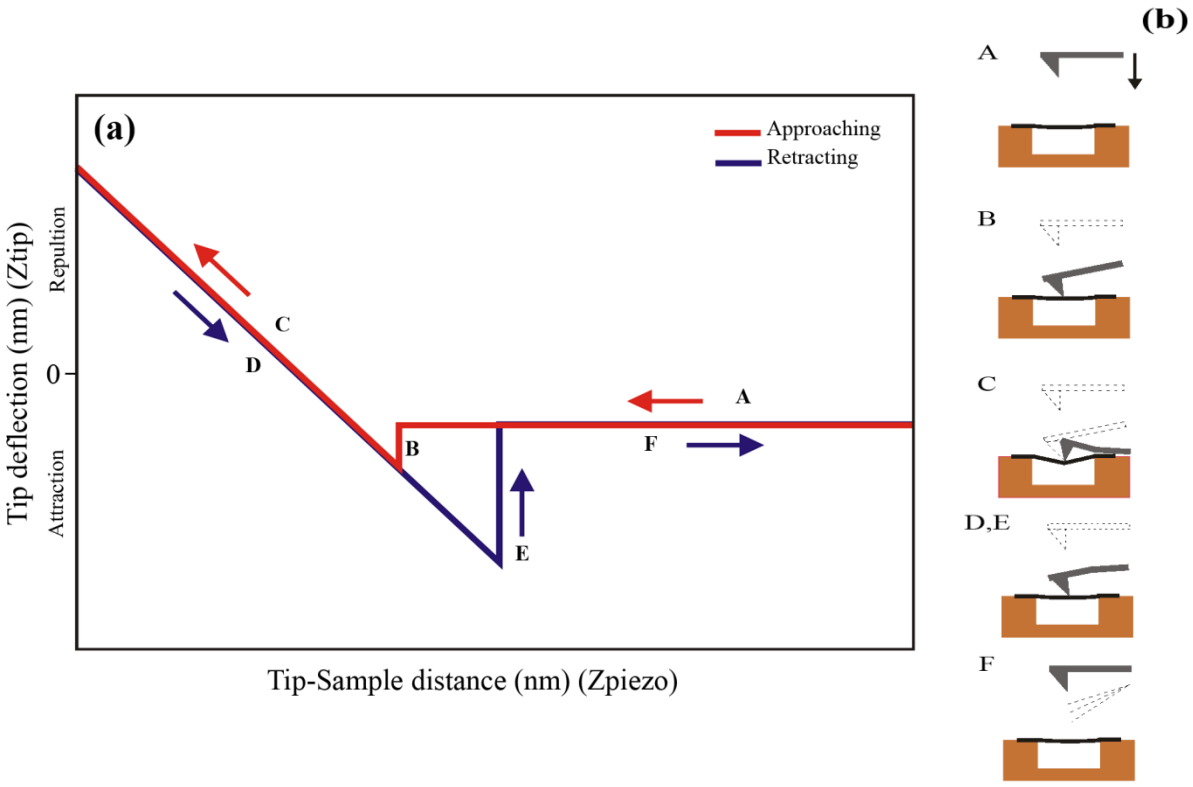

Figure 4.10- (a) A force-distance curve of the AFM in approaching and retracting regime. (b) Schematic illustration of the interaction of the tip and the sample in approaching (A- C) and retracting (D-F) regime.

Here it is explained in detail that what happens to the tip at every step while recording a force-distance curve [90]:

At the beginning the piezo extends in order to bring down the tip (A); here there is no interaction with the surface yet because of the large distance between the tip and the surface. At some point the tip is pulled down by attractive Van der Waals forces near the surface (B). After that because the piezo is still bringing down the tip, the tip applies a force and pushes the surface (C). This leads to the sample indentation and the cantilever upward deflection. This step continues till the cantilever deflects to a threshold value. Then the piezo retracts, and the cantilever reaches to the zero deflection, afterward the cantilever bends downward as the surface attraction holds the tip (D). It continues until the tip forces are in equilibrium with the surface forces. By continuing the

retraction of piezo, at some point spring constant of the tip overcomes the surface attraction and separates the tip from the surface and cantilever rebounds sharply upward (E). Later the tip ascents because the piezo continues retracting, but there are no further interaction with the tip and the surface.

One of the important properties that force-distance curve reveals, is the material's elasticity. In our case the most interesting parts of the force-distance curve are the steps C and D because the tip is in constant contact with the sample and applies a force on it. Here it is shown that the slope of the force-distance curve in these steps is used to calculate the compliance of the flake. i.e. in step C, the more the tip is pressed onto the material, the more the deformation is induced to the membrane under it. Consequently, according to the stiffness of the membrane, the cantilever bends upward in response to the restored forces on the membrane which are caused by the deformation. In Fig.4.11 the deflection of the cantilever (Z_{tip}), the deformation of the flake (U) and the distance between the tip and the sample (Z_{piezo}) are shown schematically. By using Hook's law it is possible to calculate the applied force from the deflection of the tip.

$$F_{tip} = -K_{tip} \times Z_{tip} \qquad (4.4.1)$$

Here K_{tip} is the spring constant of the tip which is measured by the force calibration method (explained in Sec.4.6). In this case the force should be small enough to keep the deformation of the flake in the linear regime; otherwise the Hook's law is not applicable.

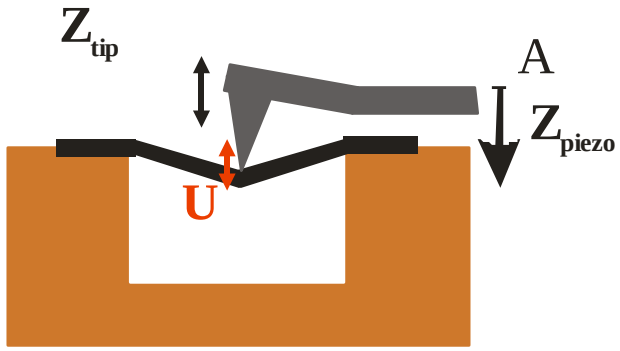

Figure 4.11- Schematic illustration of the tip deflection (Z_{tip}), the flake deformation (U) and the tip-sample surface (Z_{piezo})

In Fig. 4.11 point A shows the position of the cantilever when it is in contact with the tip but no force is applied and consequently no deformation is induced to the flake yet. In continue, as the piezo brings the sample up and consequently the tip approaches the surface from point A,

Z_{piezo} decreases and meanwhile causes the deformation of the flake and the deflection of the cantilever. As a result, the deformation is calculated from:

$$U = Z_{tip} - Z_{piezo} \quad (4.4.2)$$

in Equ. 4.4.2, when $Z_{piezo} = 0$, the maximum tip deflection occurs and the retracting regime will start.By knowing the amount of the applied force and the deformation of the flake for a given amount of the downward tip motion it is possible to calculate the compliance of the flake:

$$K^{-1} = -\partial U / \partial F_{tip} \quad (4.4.3)$$

equation 4.4.4 is achieved by replacing equations 4.4.1 and 4.4.2 in 4.4.3, in this formula $S = dz_{tip}/dz_{piezo}$ is the slope of the force distance curve.

$$K_F{}^{-1} = -dU/dF_{tip} = K_{tip}{}^{-1}(S^{-1} - 1) \quad (4.4.4)$$

hence by Equ. 4.4.4 it is shown that how the compliance of the flake is calculated directly from the inverse of the slope of the force-distance curve. As it is explained before the slope of the force distance curve on the step C is used in Equ. 4.4.4. According to this equation there is an inverse relation between the force-distance slope and the compliance of the flake. Thus the more is the slope, the smaller is the compliance and the less is the induced deformation (U) and vice versa.

For extracting all the mechanical properties of a membrane the compliance of a single point of the flake is not enough [89]. Therefore, in order to have a profile of the compliance over the surface, the data should be taken across the surface. Force-volume technique is one of the techniques to measure the elasticity at multiple points on a surface and construct a map of the local compliance over the scanned area.

Here it is necessary to mention that as it is explained in Sec. 4.5 the tip deflection is related to the associated AFM photodiode voltage by a constant called sensitivity. As a result, the tip deflection voltage versus the tip-sample distance can also be considered as a force-distance curve which is the case in this research.

During the force-volume technique voltages for each force-distance curve are recorded by AFM which are used by a program called Mega to reconstruct it. In the next section it is explained in detail. However, it is mentioned in Sec. 4.2 that the voltages that are recorded by AFM cannot be used directly for measuring piezoresistivity because it does not contain conductivity for each sample point. Consequently, in order to combine the results of the force-volume technique with the electrical properties of the flake the voltages are measured also by

ADwin. As later in this chapter more explanations are given, similar to reconstruction of the height image, we made a program in Matlab to reconstruct the force-volume results from the ADwin data and merge them with the electrical properties. As a result, the Mega program is only used to confirm that the curves that are given by the program are precise.

4.4.1. Reconstructing The Force-Distance Curves From Data Measured With AFM

The recorded voltages of AFM for force-volume technique are saved in a data file and contain the voltages of piezo in x, y and z direction and the tip deflection. These voltages are used to reconstruct the force-distance curve for each sample point by a program called Mega. Mega is a package of programs made in Matlab which can read out AFM output data file. This package is designed by molecular electronic and devices (MED) group in TU Delft. By this program it is possible to calibrate the sensitivity of the photodiode to the tip deflection (Sec 4.5) and plot the force-distance curve or the flake deformation versus tip deflection at every sample point. In Fig. 4.12 a force-distance curve is plotted for a sample point which is on the hard substrate by Mega.

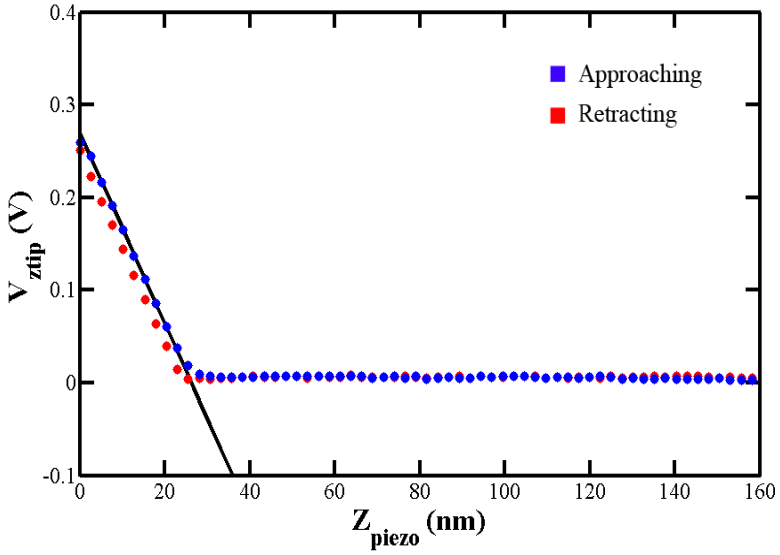

Figure 4.12 – Force-distance curve of a hard substrate plotted by Mega program from the voltages recorded by AFM

It is explained before that the more the tip applies a force on the flake to deform it, the more is the tip deflection. So the tip deflection is a measure of the applied force. The amount of the

deformation of the flake cannot be derived directly from the force-distance curve. Therefore, U vs. Z_{tip} is plotted to depict how much the flake is deformed while the force is increased. One of the samples of these graphs is illustrated in Fig. 4.13 for a sample point on the hard substrate by Mega.

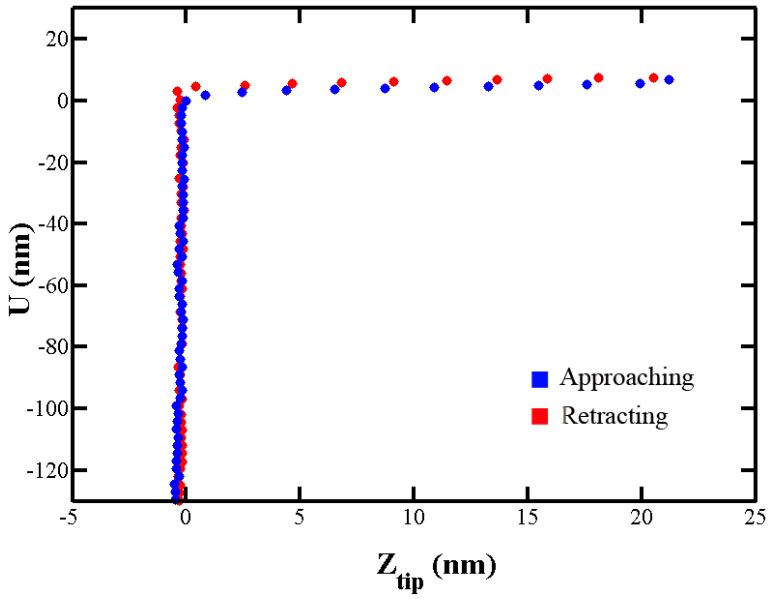

Figure 4.13 – The deformation of a hard substrate vs. the tip deflection plotted by Mega program from the voltages recorded by AFM

.

In this figure it is seen that at first the tip deflection is zero while the deformation is negative and it starts to increase as soon as the deformation starts to become positive. The reason of having such a graph is that when the tip is far from the surface, its deflection is zero and Eq. 4.4.2 yields to a negative value of U. This should, however, not be interpreted as the physical deflection of the flake as the flake and the tip do not touch. It is however convenient to include this part of the data in the plot of U v.s. Z_{tip} as it gives information about the approaching regime of the force-distance curve that would otherwise be lost. In the case of Fig. 4.13 the deformation is approximately zero which shows that the membrane is so stiff that cannot be deformed by the applied force.

As Mega program uses the data recovered by the AFM, its results are accurate. Consequently it is used to confirm the accuracy of the results achieved from the ADwin data. Later, at each step the results of Mega are discussed and compared with the results of our program.

In the next section it is focused more on the tip motion in force-volume technique and it is explained how a program is made in Matlab to reconstruct the force-distance curves from the AFM voltages.

4.4.2. Reconstructing The Force-Distance Curves From Data Measured With ADwin-Gold USB

During the force-volume measurement of the devices, the voltages of x, y, z piezo and the tip deflection, plus the conductivity of the flake are measured and recorded through ADwin-Gold USB by time trace software, every millisecond (Sec. 4.2). According to the scan rate of AFM in our setup each force volume measurements takes about one hour. During this time, ADwin measures about 3.1×10^6 points which is much more than AFM data points. Like it is explained in Sec.4.3.1 the ADwin data contains the information of the sample points and also the electrical noises. Consequently, in order to reconstruct the force-distance curves from the ADwin data, we made a program in Matlab which is explained here in detail:

When performing the force-volume technique in tapping mode, at each sample point the piezo scanner keeps the position of the tip at a fixed x and y position while the AFM records the force-distance curve of that point. Afterwards, when the tip is retracted, the piezo continues the xy motion (Fig. 4.6) till the next sample point. It means that the tip remains for a longer time at each sample point and the x and y piezo voltages are approximately the same during the approaching and retracting regime. As it is shown schematically in Fig. 4.14, such motion makes a step for each sample point at the voltage of piezo in x and y direction.

The complication of such motion is that the length of the step is not the same at every point because the tip has to move further up or down to obtain the same tip deflection as the surface height changes.

The first part of the program is to find the voltage of x piezo at each step. In Fig. 4.14 point A and B show the points in the middle and end of one step respectively. Point C shows the first point of the next step. By comparing the voltages of these points, it is clearly seen that there is a significant difference between the voltages of points B and C. In contrast, the difference between the voltage of points A and B which are at the same step is small. This fact can be used to find the first point of each step. The voltage of x piezo is checked in an interval of approaching and retraction motion of the tip (average length of the steps). In this interval the times of the two

voltages that have the maximum difference compared to the other points are selected as the time of finishing the current step and starting the next step respectively. When the times of the first and last point of each step are found, it is possible to determine the value of average x and y piezo voltage and the tip deflection voltage plus the average conductivity for each step. With this information, we are able to separate the individual force-distance curves.

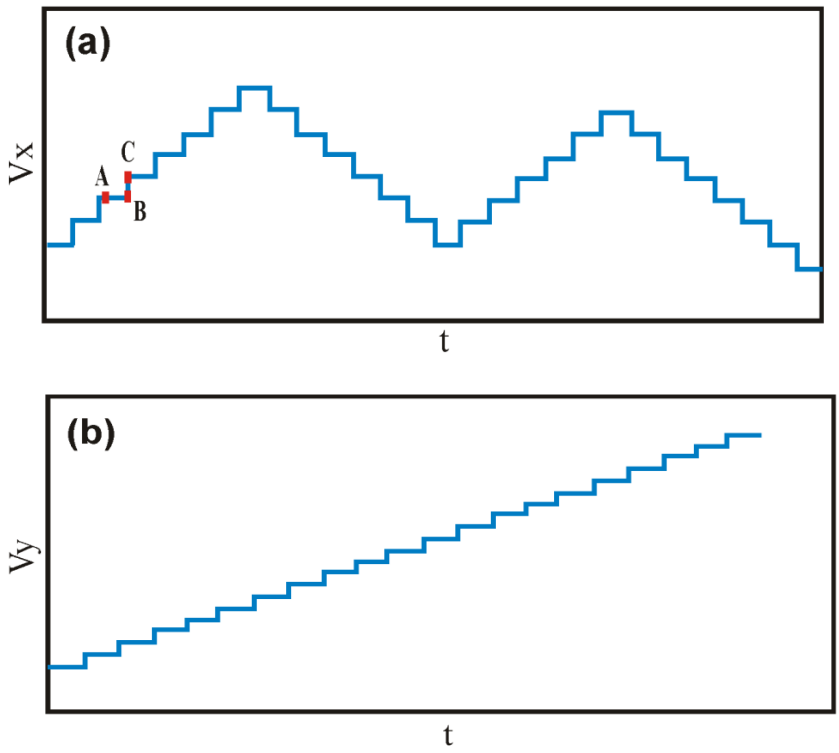

Figure 4.14 – Schematic motion of (a) x and (b) y piezo voltage in force volume technique, in reality the length of the steps are not the same at every point because the time that each force-distance curve takes depends on the height of the surface.

In the next part, the designed program separates the values of the voltages for approaching and retracting regime of the tip for each step. The tip-sample distance and the tip deflection voltages vs. time are shown schematically in Fig. 4.15. In Fig. 4.15.a as the z piezo voltage is reduced, the tip approaches the surface, thus the minimum value is the interface between the approaching and retracting regime. It is shown in Fig. 4.15.b that at the moment when the tip-sample distance reaches to its minimum the maximum of the tip deflection and the change in the resistivity occurs. In the program, the index of the minimum value of the tip-sample distance is determined along each step to distinct the approaching and retracting regime.

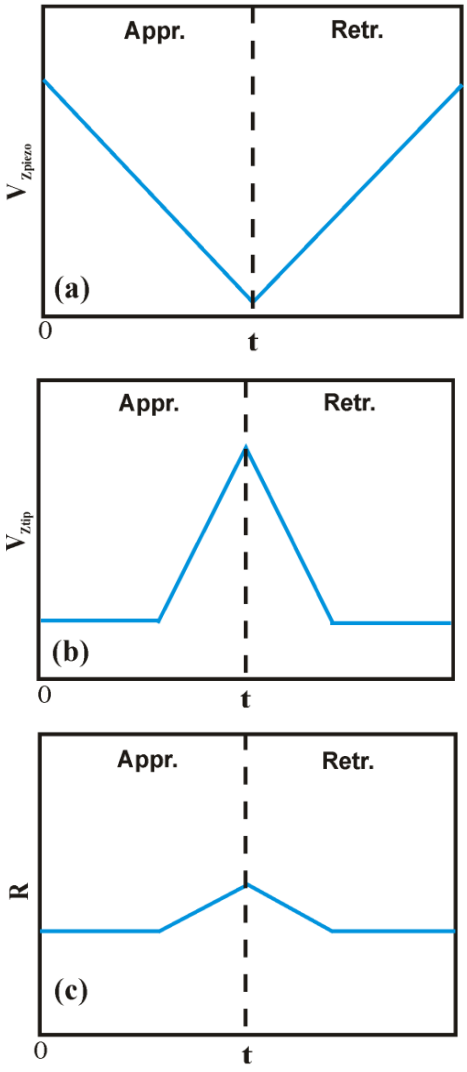

Figure 4.15- Changes of (a) the piezo voltage in z direction, (b) tip deflection voltage (c) the resistivity (which can either increase or decrease depending on gauge factor (GF) of the device), vs. time during the recording of force-distance curve

Afterward, it is possible to calculate the tip-sample distance and the tip deflection using the sensitivity and consequently the deformation of the flake by equation 4.4.2 for each step, separately for approaching and retracting regime. When all the data for each sample point are obtained separately, we can plot the force-distance curve for each point. Fig. 4.16.a depicts a force distance curve for a sample point which is plotted by our program. In this plot the values of the approaching and retracting regime are shown with different colors and the steps of the force-distance curve that are explained in Sec. 4.4 are visible. Besides, a line is fitted to the step C of

the force-distance curve (Sec. 4.4) in order to find the slope of the force-distance curve. Then the compliance of the flake is calculated according to Eq. 4.4.4.

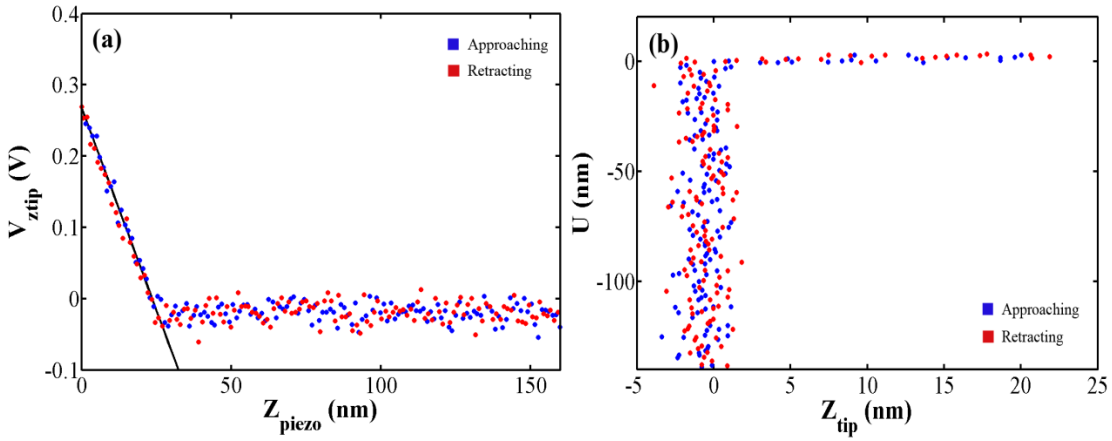

Figure 4.16- (a) The force-distance curve, (b) induced deformation vs. tip deflection, plotted by ADwin data, for a point on the substrate

In Sec. 1.3 the piezoresistivity is explained and it is explained that the Gauge Factor (GF) which is defined by Equ. 1.3.3 is usually used to measure this property. In this equation it is shown that:

$$GF \approx \Delta R/\varepsilon$$

as the calculation of the induced strain on the flake in our case is complicated and needs more simulations, in this research instead of calculating GF, we try to show the piezoresistive behavior of graphene by considering the factors that are related to the strain and cause the changes in the resistance. In other word, as:

$$\varepsilon \approx \sigma \approx F \qquad (\sigma\text{: stress, F: applied force})$$

we can investigate the effect of the factors that change the applied force. One of these factors is Z_{piezo}, from the force distance curve it is clear that when the tip touches the surface, by reducing Z_{piezo} the applied force increases and causes the deformation and induces strain. Consequently, in our case the slope of the R vs. Z_{piezo} is used as a symbol of GF to show the piezoresistive behavior of graphene.

Plotting ΔR versus the Z_{piezo} for each sample point is derived from the ADwin data. It is shown in Fig.4.17 for an approaching regime. The slope of this plot from the point that the tip deflection starts, can show the trend of changes in GF. These plots are used to make the profiles of the flake properties over the surface.

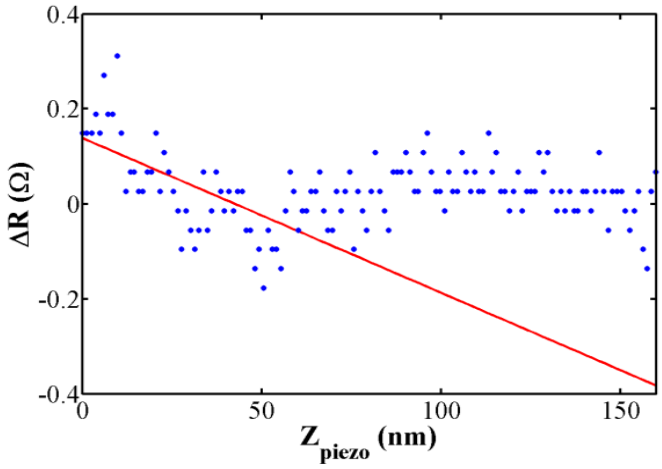

Figure 4.17- Change in resistivity vs. tip-sample distance for approaching regime for a sample point plotted by ADwin data

In order to get the profiles of the height, compliance and changes in the resistivity, first the slope of the force-distance curve is used to calculate the compliance of the flake at each sample point. Furthermore, the compliance values are fitted over the grid of the surface with the same method as the height value explained in Sec. 4.3.1. After that the slope of the changes in resistivity versus Z_{pieoz} is determined for each sample point and its profile is plotted over the surface. The reason of using the slope of the resistivity changes is that in our case the changes in the resistivity are so small; to show the changes more precisely the slope is used instead of ΔR. All the mentioned profiles are illustrated in chapter 5.

4.4.3. Comparing The Results Taken From AFM Data With The Results of ADwin-Gold USB Data

As it is mentioned before the voltages measured by AFM can be used as a source to prove that the program which we have made works properly. In this section, the curves that are plotted for different sample points with AFM and ADwin data are compared together.

Fig. 4.18 (a-d) depicts the force-distance curves and the deformation versus the tip deflection for a sample point of the flake on the hard substrate plotted by ADwin and AFM data.

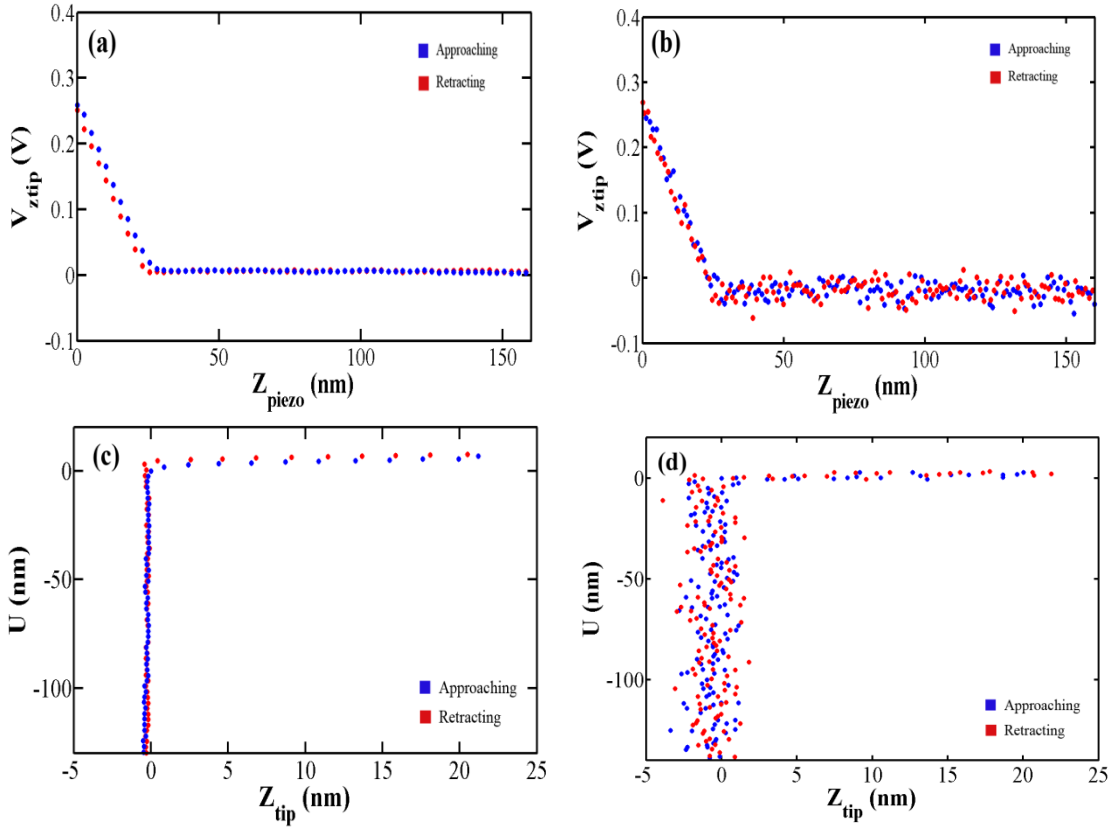

Figure 4.18 - (a) The force-distance curve plotted by AFM data, (b) The force-distance curve plotted by ADwin data, (c) U vs. Z_{tip} plotted by AFM data and (d) U vs. Z_{tip} plotted by ADwin, for a point of the flake on the hard substrate

From Fig. 4.18. it is clearly seen that in both a and b the tip deflection starts at the same height above the surface and also the slopes of the force-distance curve and the maximum tip deflection are almost the same. The deformation of the flake in c and d is also the same and is almost zero. In general the results which are derived by ADwin data match very well with the results of AFM data. But there are also some differences. One of the differences is the number of points in the results of ADwin. The reason is that the number of points that ADwin measures are more than AFM and this is because of the difference in their sampling rate; i.e. in our case, the sampling rate for AFM is set to be around 77 per seconds while for ADwin is around 1000 per seconds. So the number of measured values by ADwin is about thirteen times more than AFM. The other difference is a small variation in the value of the voltages in ADwin compared to AFM which is the result of the electrical noises and some approximations in the program that are explained before. However, the effect of these differences is small and can be ignored.

In fig.4.19 the same plots as fig.4.18 are illustrated for a point of the flake which is on the center of the hole. It is seen that the slopes of the force-distance curves and U vs. Z_{tip} are almost the same in a and b, and c and d respectively. The deformation also starts at the same height in the plot of AFM and ADwin.

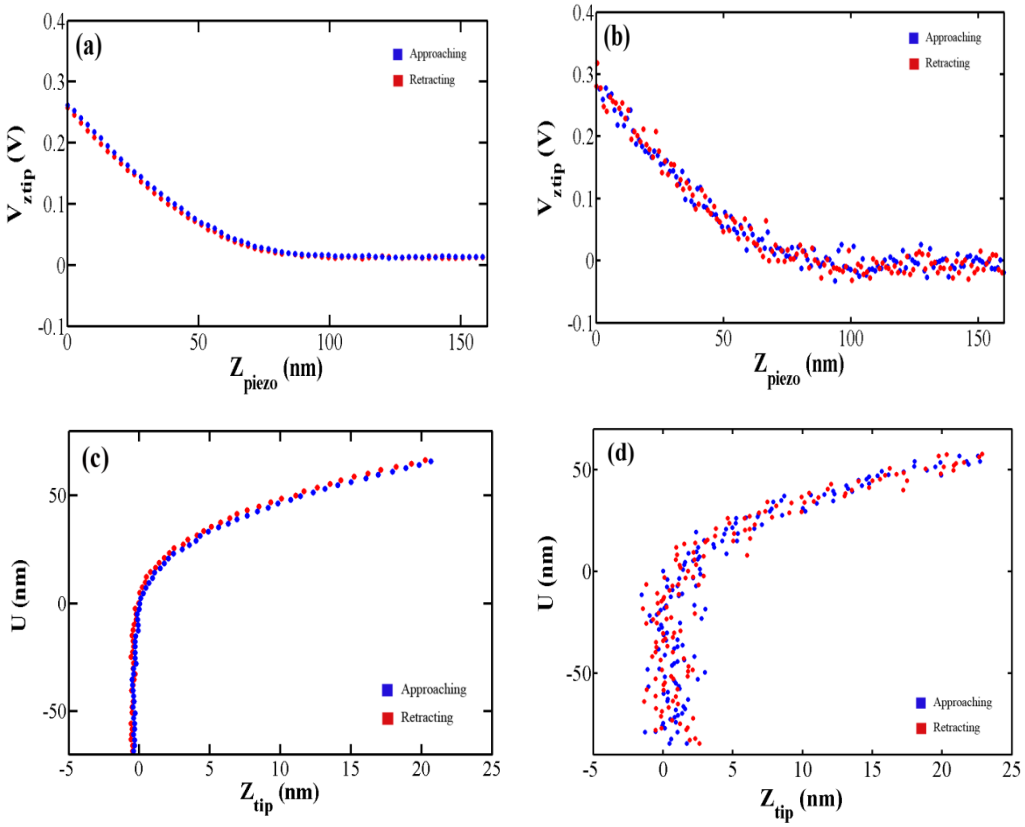

Figure 4.19- (a) The force-distance curve plotted by AFM data, (b) The force-distance curve plotted by ADwin data, (c) U vs. Z_{tip} plotted by AFM data and (d) U vs. Z_{tip} plotted by ADwin for a point of the flake on the center of a hole

By comparing the results of ADwin with AFM, it is proved that the measured voltages with ADwin can be used reliably for the determination of the applied force by the AFM tip and the deformation of the flake.

4.5. Tip Deflection Sensitivity

The voltages that are measured by AFM or ADwin for the tip deflection can be converted to Z_{tip} by a constant factor called the tip deflection sensitivity. It represents the cantilever deflection

signal (V_{ztip}) versus the deflection of the tip in Z direction (Z_{tip}). In other words, it shows if the cantilever deflects one nanometer, how much the tip deflection voltage will change.

$$V_{ztip} = Sensitivity \times Z_{tip} \tag{4.5.1}$$

The tip deflection sensitivity is achieved by the calibration. The calibration of the sensitivity is necessary in order to derive accurate data from force-distance plots. For calibration a force-distance image is taken on the hard substrate. Because the substrate cannot be deflected by the tip (i.e. U = 0 in Eq. 4.4.2), the tip deflection is equal to the extension (or compression) of the z piezo tube ($Z_{tip} = Z_{piezo}$). So the slope of the force-distance curve is used to extract the tip deflection sensitivity.

In order to do the calibration, first a force-volume image is taken by AFM on the silicon substrate. Then the slope of the force-distance curves are determined for every sample point; and as depicted in Fig. 4.20, the slopes are illustrated with a histogram, and their average is considered as the average of the tip deflection sensitivity (Table 4.1). To be more precise, in our case, it is done for approaching and retracting regime separately and their average is used as the tip deflection sensitivity.

The calibration is done by both AFM and ADwin data and their results are compared together. The results are depicted in Fig. 4.20 and table 4.1. One should pay attention that the data ranges of the histograms are not the same for AFM and ADwin. The histograms of Fig. 4.20 show the scattering of the range of the slopes for force-distance curves in each regime. The wider are the histograms the more scattered are the range of the slopes.

A small difference in the sensitivity achieved by AFM data compared to ADwin is acceptable because in AFM we have the exact data of sample points, but in ADwin there are also some electrical noises which can lead to a larger uncertainty in the results.

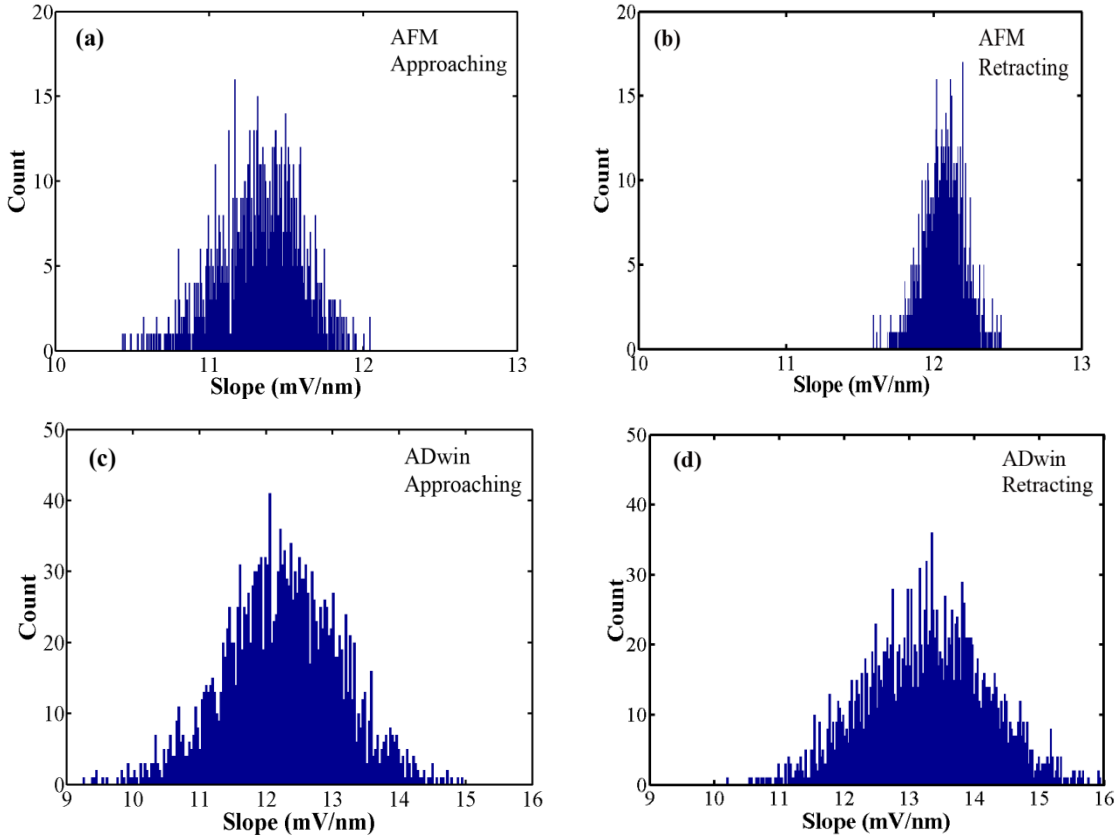

Figure 4.20- The histogram of the tip deflection sensitivity for approaching and retracting regime respectively derived from AFM and ADwin output data

Table 4.1- the average tip deflection sensitivity for approaching and retracting motion of the tip

	AFM data	**ADwin data**
Approaching sensitivity (mV/nm)	11.5 ± 0.1	12.2 ± 0.8
Retracting sensitivity (mV/nm)	12.1 ± 0.1	13.2 ± 0.9
Average of the tip deflection sensitivity (mV/nm)	11.8	12.7

For analyzing the data of each source (AFM or ADwin) we use its own sensitivity to get the more precise results. The accuracy of the results depends on the accuracy of the designed program and the tip deflection sensitivity calibration. In addition to that it is necessary to

determine the spring constant of the cantilever in order to calculate the applied force. This is done by a method called force calibration which is explained in the next section.

4.6. Force Calibration

Reliable results of the applied force from the measured voltages of the AFM tip deflection require an accurate calibration of the spring constant of the tip. There are several methods to estimate the spring constant of a tip such as reference cantilever method [84], theoretical methods according to cantilever geometry and materials and thermal noise method [84].

In this research we have used the thermal noise method to calculate the spring constant of the tip, but the values that was achieved does not seem logical, as a result at the end the values that are reported by the manufacturing company of the tips which in our case is 42-46 Nm^{-1}, is used to calculate the applied force.

Chapter 5

Results and discussions

After preparing all the requirements of measuring the piezoresistivity with our method, it is possible to measure the devices. In this thesis the piezoresistivity of two flakes with the average thickness of 3 nm (measured by AFM) which means that the flake has about 10 layers of graphene are measured. In general, they both showed the same behavior.

In order to measure, first the device is placed on AFM and connected to the electrical setup. Furthermore its electrical conductivity is checked to be sure that the device is conductive. Then the height image technique is used to focus on top of the hole. After that the force-volume measurement is taken while a bias voltage is applied to the device and meanwhile the conductivity of the device is recorded. In this chapter, first it is explained that how the conductivity of the device is checked and then the results of one of the devices is discussed.

5.1. Checking the Connectivity Of The Devices

Before doing the AFM measurements, the conductivity of the device is checked by measuring the resistance and its changes according to the bias and gate voltages. The device which its results are reported in this chapter is depicted in Fig. 5.1. In this nanodrum the diameter of the hole is 1µm and as mentioned above the average thickness of the flake is 3 nm. In this device the distance between the electrodes around the drum is around 2µm.

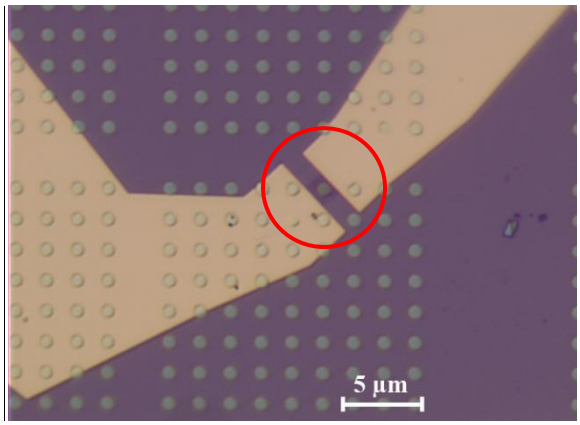

Figure 5.1- The measured nanodrum with gold electrodes, the diameter of the hole is 1µm and the thickness of the flake is 3nm.

The resistance of the device is determined by measuring its IV curve. Fig. 5.2 depicts the IV curve of the device in Fig. 5.1. It is seen that the device has a linear IV curve with a resistance of about 3.5 kΩ.

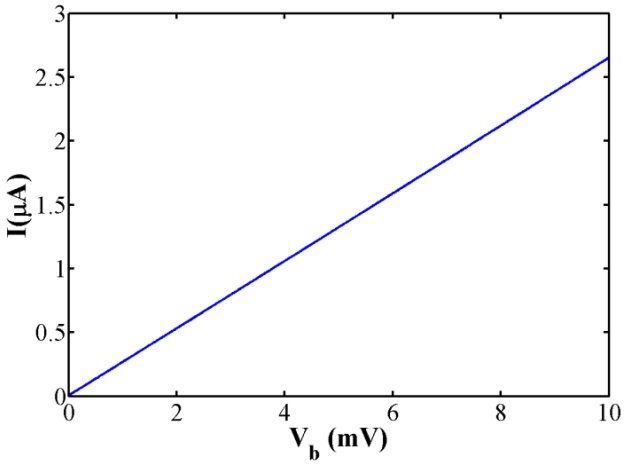

Figure 5.2- IV curve of one of the nanodrums which is a linear and shows a resistance around 3.5 KΩ

In the next step the gate dependence of the device is checked in a way that a fixed bias voltage is applied and the gate voltage is changed. The means of this test is to see if the electric field caused by the gate voltage can change the band gap of the graphene layer by changing the distance between the layers and consequently affect its resistivity or not. In general significant gate dependence is expected for single layer and few layers graphene ($n < 3$), but if the number of layers increases the gate dependence disappears [27]. In our case to see if the conductance is gate dependent a small bias voltage (10 mV) is applied and the gate voltage is swept from -8 to +8 V. According to the results (i.e. Fig. 5.3), in all of our devices no gate dependence is observed. The reason is the thickness of the flakes, because the flakes are around 10 layers, so no gate dependence is shown.

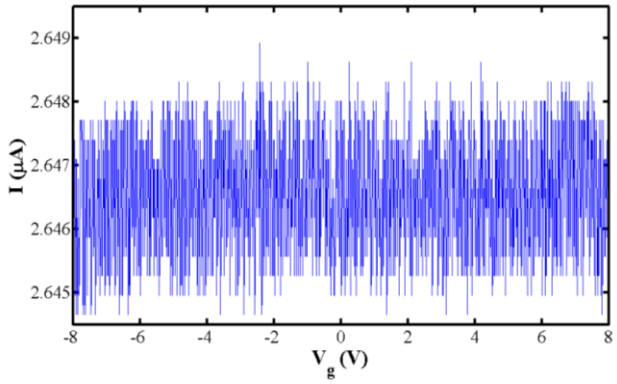

Figure 5.3 – The plot of current vs. gate voltage to check the gate dependence of the conductance

These measurements illustrates that the device shows ohmic behavior with no gate dependence. In the next section the results of the force-volume measurements and the piezoresistivity of one of the devices are illustrated and discussed.

5.2. Results Of The Piezoresistivity

5.2.1. Individual Sample Point Measurements

After it is shown that the device is conductive a height image is taken off the area of the drum which is depicted in Fig. 5.4. In this image, point A shows a part of the flake which is on the hard substrate and point B shows a part of the suspended flake which is on the center of the hole. The darker color which is more significant by approaching the center of the hole illustrates that the flake is more suspended on the center compared to the edges of the hole, the bright triangle on top right is related to the electrodes that are formed around the hole

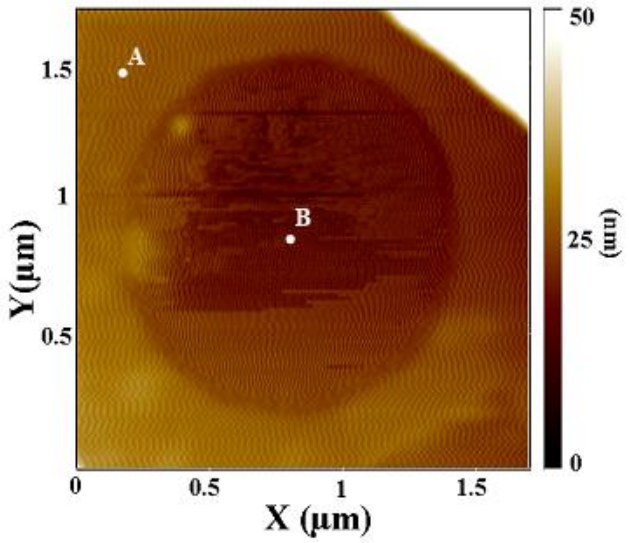

Figure 5.4- AFM height image of a nanodrum, the darker color which is more significant by approaching the center of the hole illustrates that the flake is more suspended on the center compared to the edges of the hole, the bright triangle on top right is related to the electrodes that are formed around the hole

After the height image the bias voltage is applied to the source and the drain and finally the force-volume measurement is started. Fig. 5.5 depicts the reconstructed force-distance curves and the deformation versus the tip deflection for the points A and B of the device which is shown in Fig. 5.4.

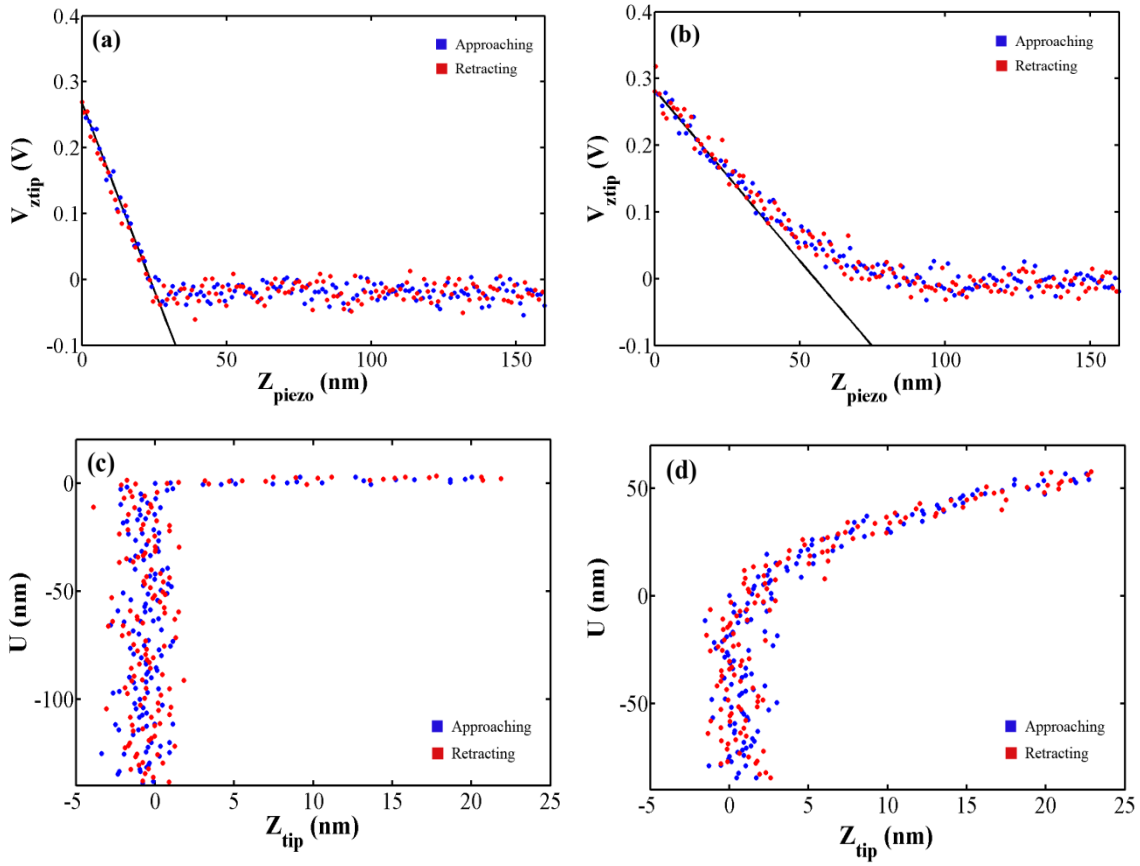

Figure 5.5 – (a) The force-distance curve of a point A on the hard substrate, (b) The force-distance curve of a point B on the flake on the center of the hole, (c) U vs. Z_{tip} of a point A on the hard substrate, (d) U vs. Z_{tip} of a point B on the flake on the center of the hole.

By comparing the plots of Fig.5.5.a with the one in Fig.5.5.b, it is clearly seen that the plots are more rounded for the point on the center of the drum than the substrate. Besides, the slope of the force-distance curve in step c in Fig.5.5.b is less than Fig.5.5.a. According to Equ. 4.4.4. it shows that the flake is more deformable on the center of the hole compared to the top of the substrate. Consequently when the force is applied by the tip, the flake applies less force on the cantilever to bend it upward. And the maximum tip deflection is achieved gradually. The amount of the deformation of the flake is determined from Fig.5.5.c and d. In these plots it is seen that for the case of the substrate no deformation is achieved by increasing the tip deflection (or force). In contrast, the deformation of the flake is achieved up to 50 nm by applying the force and increasing the tip deflection in the center of the hole.

Fig. 5.6.a illustrates the effect of the deformation on the resistance of the flake. Fig. 5.6.a depicts that when the flake cannot be deformed because it is on the hard substrate the change in

the resistance (ΔR) is all the time around zero. It means that the approaching of the tip does not change the resistance and it is the same during the force-distance measurements. In our case ΔR is not exactly zero because of some environmental noises that cannot be avoided but tried to be reduced as much as possible, but it does not affect the results as we are measuring ΔR not the R and the amount of the noises are fixed. But in Fig. 5.6.b, it is clearly seen that the resistance increases as soon as the flake is deformed and the tip deflection starts. The amount of the change in this case is increasing the resistance about 200 mΩ which is small compared to the total resistance of the flake. As it is mentioned before the data derived from every single plot is used to make the profiles of the measured properties. These profiles are depicted in the next section.

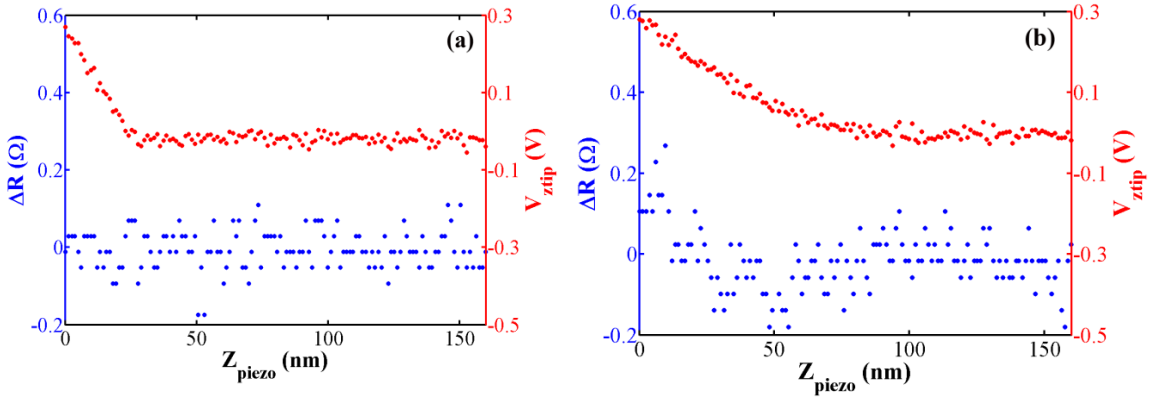

Figure 5.6 – The tip deflection (red) and change in the resistance (blue) vs. tip-sample distance for (a) point A on the hard substrate, (b) point B on the flake on the center of the hole

5.2.2. Profiles Of The Mechanical Properties And the Resistance

It is explained in Sec.4.4.3 that in order to have the average value of all the changing properties of the membrane, their profiles are plotted over the surface. In this section the profiles that are achieved for the device of Fig. 5.4 are explained. These profiles are plotted in Fig. 5.7.

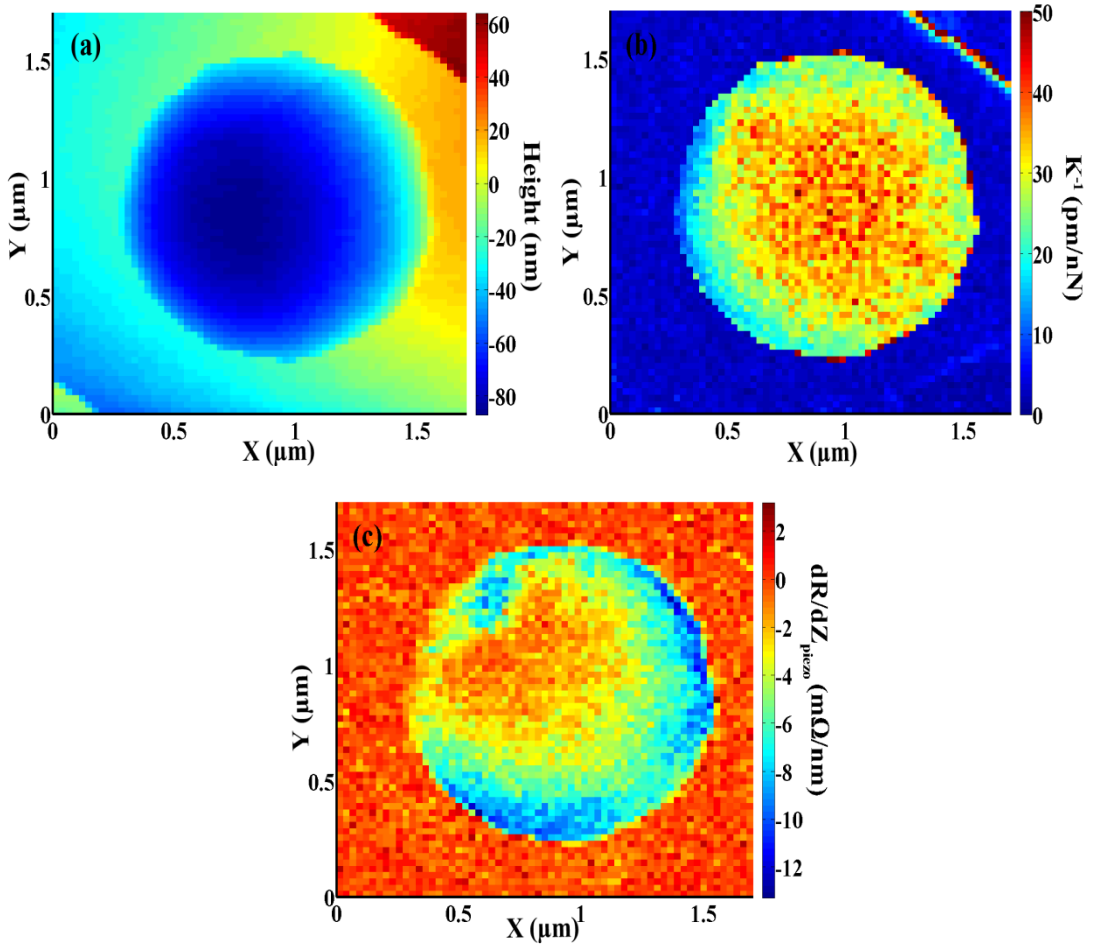

Figure 5.7 – (a) The height profile, (b) the compliance profile, (c) the slope of the R vs. Z_{piezo} profile of a 3 nm graphene flake suspended on top of a 1 µm hole.

The first image (Fig. 5.7.a) depicts the height profile of the drum. It is clearly seen that the flake is more deflected on the center of the drum; like what is observed in the height image of the device (Fig. 5.4). The flake is clamped on the edge of the hole but by going far from the edges and approaching the center of the drum the deflection increases. This deflection is not because of the applied force and it always happens because of the weight of the flake. Fig. 5.7.b illustrates the profile of the compliance of the flake. It is derived from the image that by approaching to the center of the flake, its compliance increases. Consequently, the flake is more deformable when it is more deflected on the center. In Sec. 2.6 the theoretical studies that have been done on the compliance of the graphene nanodrums [2] is explained. There is an agreement between the experimental results which are shown in Fig. 5.7 and the theoretical studies. The line on the top

right corner of the image which shows the sudden change in compliance appears because of the slipping of the tip from the edges of the contacts.

In Fig. 5.7.c, the profile of the slope of the R vs. Z_{piezo} over the surface is shown. By a quick look, this image reveals that graphene shows the piezoresistive behavior because the resistivity changes according to deformation of the flake. According to Fig. 5.7.c when the flake is deformed by the tip the slope of the R vs. Z_{piezo} reduces more significantly at the edges of the hole compared to the center. It means that by deforming the flake the resistance changes more in the edges and as we approach the center while the deformation of the flake increases the change in the resistance decreases. This is in contrast with what we have expected and what predicted (Sec. 1.3.1). According to theoretical studies increasing the deformation should increase the piezoresistivity; as a result, as the flake is more deformable on the center of the flake (Fig. 5.7.b) it should show more changes in the resistance as we approach the center. The reason of such contrast needs further investigations and theoretical modeling. There are different factors that can play a role such as the amount of the applied force or the stress at the clamping point. Without investigating all these factors it is not possible to give a certain reason for such behavior ofgraphene.

Conclusions

The focus of this thesis is on measuring the piezoresistive behavior in graphene in the form of nanodrum. To the best of the author's knowledge, this has been done here for the first time since experimental studies of piezoresistivity of graphene have not been reported yet in the literature.

The experimental results show that the flake used in the devices displays an Ohmic behavior with an electrical resistance of 3.5 KΩ. The suspended flake it is more deformable on the center of the hole compared to the edges. By consequence, the compliance is larger in the center of the nanodrum. Moreover, the change in the slope of ΔR vs. Z_{piezo} plots (used as a parameter to show the trend of changes in the gauge factor, GF) show that GF decreases with increasing the deformation. This could be due to not applying a sufficient force to the graphene flake and will require subsequent investigation.

According to our results, certainly graphene shows the piezoresistive behavior. This property makes few layer graphene nanodrums ideal candidates for pressure or mass sensors (at individual molecule scale).

In summary, we have shown that AFM measurement of electrical and compliance profile of the suspended flake can give information on the piezoresistive behavior of graphene. The method is very promising and will certainly benefit from further optimization of the experimental conditions. (i.e. optimizing the applied force, reducing the electrical noise, etc.). For further work we recommend to optimize the measurement setup and the thickness of the flake (for example fabricate the single flake). Furthermore investigating the effect of the amount of forces or diameter of the holes on the changes of the resistance of the single flake should reveal interesting information about the piezoresistivity of the graphene.

Acknowledgement

We thank Gregory Schneider, Samir Etaki, Ferry Prins, Mascha Van Oossanen, Amelia Barreiro, Liu Xinglan for their help with sample fabrication and consultancies. This thesis is supported and done in the Molecular electronics and devices (MED) group in the department of Applied Science in Technical University of Delft (TUDelft).

References

1- M. Roukes, Nanoelectromechanical systems face the future, Physics World Magazine, Vol. 14, No. 2 (2001).

2- M. Poot, Mechanical systems at the nanoscale (Casimier PhD Series, Delft-Leiden 2009).

3- M. Poetschke, C. G. Rocha, L. E. F. Foa Torres, S. Roche, and G. Cuniberti, Modeling graphene-based nanoelectromechanical devices, Physical Review B, Vol. 81, 193404 (2010).

4- L. Yong, W. Wanlu, L. Kejun, H. Chenguo, H. Zhi, and F. Qing, Piezoresistive effect in carbon nanotube films, Chinese Science Bulletin, Vol. 48, No. 2, 125-127 (2003).

5- R. J. Grow, Q. Wang, J. Cao, D. Wang, and H. Dai, Piezoresistance of carbon nanotubes on deformable thin-film membranes, Applied Physics Letters, Vol. 86, 093104 (2005).

6- M. V. Medvedyeva, and Ya. M. Blanter, Piezoconductivity of gated suspended graphene, arXiv: (cond-mat) 1006.5010 (2010).

7- M. L. Roukes, Nanoelectromechanical systems, Technical Design of the 2000 Solid-State Sensor and Actuator Workshop, Hilton Head IsI., SC (2000) - ISBN 0-9640024-3-4.

8- J. C. Meyer, A. K. Geim, M. I. Katsnelson, K. S. Novoselov, T. J. Booth and S. Roth, The structure of suspended graphene sheets, Nature, Vol. 446, 60-63 (2007).

9- A. C. Ferrari, J. C. Meyer, V. Scardaci, C. Casiraghi, M. Lazzeri, F. Mauri, S. Piscanec, D. Jiang, K. S. Novoselov, S. Roth, and A. K. Geim, The Raman fingerprint of graphene, Phys. Rev. Lett., Vol. 97, 187401 (2006).

10- A. K. Geim, and K. S. Novoselov, The rise of graphene, Nature Materials, Vol. 6, 183-191 (2007).

11- C. Oshima and A. Nagashima, Ultra-thin epitaxial films of graphite and hexagonal boron nitride on solid surfaces, J. of Phys.: Condens. Matter, Vol. 9, No. 1 (1997)

12- K. S. Novoselov, S. V. Morozov, T. M. G. Mohinddin, L. A. Ponomarenko, D. C. Elias, R. Yang, I. I. Barbolina, P. Blake, T. J. Booth, D. Jiang, J. Giesbers, E. W. Hill, and A. K. Geim, Electronic properties of graphene, Phys. Stat. Sol. (b), vol. 244, No. 11, 4106-4111 (2007).

13- P. R. Wallace, The band theory of graphite, Phys. Rev., Vol. 71, 622–634 (1947).

14- J. W. McClure, Diamagnetism of graphite, Phys. Rev., Vol. 104, 666–671 (1956).

15- J. C. Slonczewski and P. R. Weiss, Band structure of graphite. Phys. Rev., Vol. 109, 272–279 (1958).

16- L. D. Landau, and E. M. Lifshitz, Statistical Physics Part I, (Pergamon, Oxford 1980).

17- N. D. Mermin, Crystalline order in two dimensions. Phys. Rev., Vol. 176, 250–254 (1968).

18- J. A.Venables, G. D. T. Spiller, and M. Hanbucken, Nucleation and growth of thin films, Rep. Prog. Phys., Vol. 47, 399–459 (1984).

19- J. W. Evans, P. A. Thiel, and M. C. Bartelt, Morphological evolution during epitaxial thin film growth: Formation of 2D islands and 3D mounds, Sur. Sci. Rep., Vol. 61, 1–128 (2006).

20- Novoselov, K. S. et al. Electric fi eld eff ect in atomically thin carbon fi lms. Science 306, 666–669 (2004).

21- Novoselov, K. S. et al. Two-dimensional atomic crystals. Proc. Natl Acad. Sci. USA 102, 10451–10453 (2005).

22- Novoselov, K. S. et al. Two-dimensional gas of massless Dirac fermions in graphene. Nature 438, 197–200 (2005).

23- Stankovich, S. et al. Graphene-based composite materials. Nature 442, 282–286 (2006).

24- K. S. Novoselov, D. Jiang, F. Schedin, T. J. Booth, V. V. Khotkevich, S. V. Morozov, and A. K. Geim, two dimensional atomic crystals, PNAS, Vol. 102, No. 30, 1451-1453 (2005).

25- D. R. Nelson, T. Piran, and S. Weinberg, Statistical Mechanics of Membranes and Surfaces (World Scientifi c, Singapore, 2004).

26- S. V. Morozov, K. S. Novoselov, M. I. Katsnelson, F. Schedin, L. A. Ponomarenko, D. Jiang, and A. K. Geim, Strong Suppression of Weak localization in Graphene, Phys. Rev. Lett., Vol. 97, 016801 (2006).

27- K. S. Novoselov, A. K. Geim, S. V. Morozov, D. Jiang, Y. Zhang, S. V. Dubonos, I. V. Grigorieva, and A. A. Firsov, Electric field effect in atomically thin carbon films, Science, Vol. 306, 666-669 (2004).

28- Y. Zhang, Y. W. Tan, H. L. Stormer, and Philip Kim, Experimental observation of the quantum Hall effect and Berry's phase in graphene, Nature 438, 201-204 (2005).

29- C. Chen, S. Rosenblatt, K. I. Bolotin, W. Kalb, P. Kim, L. Kymissis, H. L. Stormer, T. F. Heinz, and J. Hone, Performance of monolayer graphene nanomechanical resonators with electrical readout, Nature Nanotechnology, Vol. 4, 861 - 867 (2009).

30- A. Geim, P. Kim, Carbon wonderland, Scientific American, 90-97, (2008).

31- M. S. Dresselhaus; G. Dresselhaus, Intercalation compounds of graphite, Adv. Phys., Vol. 51, Issue 1 (2002).

32- H. Shioyama, Polymerization in the interlayer of KC24 in the presence of organic solvents, J. Mater. Chem., Vol. 11, 3307–3309 (2001).

33- A. J. Van Bommel**a**, J. E. Crombeen and A. Van Tooren**,** LEED and Auger electron observations of the SiC(0001) surface, Surf. Sci, Vol. 48, Issue 2, 463-472 (1975).

34- C. Berger, Z. Song, T. Li, X. Li, A. Y. Ogbazghi, R. Feng, Z. Dai, A. N. Marchenkov, E. H. Conrad, P. N. First, and W. A. de Hee, Ultrathin Epitaxial Graphite: 2D Electron Gas Properties and a Route toward Graphene-based Nanoelectronics, *Phys. Chem. B*, Vol. 108, Issue 52, 19912–19916 (2004).

35- M. S. Purewal, Y. Zhang, and P. Kim, Unusual transport properties in carbon based nanoscaled materials: nanotubes and graphene, Phys. Stat. Sol. (b) 243, No. 13, 3418-3422 (2006).

36- G. W. Semenoff, Condensed-Matter Simulation of a Three-Dimensional Anomaly, Phys. Rev. Lett., Vol. 53, 2449–2452 (1984).

37- F. D. M. Haldane , Model for a Quantum Hall Effect without Landau Levels: Condensed-Matter Realization of the "Parity Anomaly, Phys. Rev. Lett., Vol. 61, 2015–2018 (1988).

38- I. Meric, M. Y. Han, A. F. Young, B. Ozyilmaz, P. Kim, and K. L. Shepard, Current saturation in zero-bandgap, top-gated graphene field-effect transistors, Nature Nanotechnology, Vol. 3, 654 - 659 (2008).

39- K. I. Boltin, K. J. Sikes, Z. Jiang, G. Fudenberg, J. Hone, P. Kim, and H. L. Stormer, Ultrahigh electron mobility in suspended graphene, Solid State Communications, Vol. 146, Issues 9-10, 351-355 (2008).

40- A. K. Geim, Graphene: statuse and prospects, Sience, Vol. 324, 1530-1534 (2009).

41- M. I. Katsnelson, Graphene: carbon in two dimensions, Materials Today, Vol. 10, No. 1-2, 20-27 (2007).

42- Y. Zhang, J. P. Small, W. V. Pontius, and P. Kim, Fabrication and electric-field-dependent transport measurements of mesoscopic graphite devices, Appl. Phys. Lett., Vol. 86, 073104 (2005).

43- K. Nakada and M. Fujita, Edge state in graphene ribbons: Nanometer size effect and edge shape dependence, Phys. Rev. B 54, 17954–17961 (1996).

44- C. Lee, X. Wei, J. W. Kysar, and J. Hone, Measurement of the elastic properties and intrinsic strength of monolayer graphene, Science, Vol. 321, 385-388 (2008).

45- J. S. Bunch, A. M. van der Zande, S. S. Verbridge, I. W. Frank, D. M. Tanenbaum, J. M. Parpia, H. G. Craighead and P. L. McEuen, Electromechanical Resonators from Graphene Sheets, Science, Vol. 315, No. 5811, 490-493 (2007).

46- B. Ilic, H. G. Craighead, S. Krylov, W. Senaratne, C. Ober, and P. Neuzil, Attogram detection using nanoelectromechanical oscillators, J. Appl. Phys., Vol. **95**, 3694 (2004).

47- The Royal Schwedish Academy of Science. Scentific Background on the Nobel Prize in Physics (2010).
(http://nobelprize.org/nobel_prizes/physics/laureates/2010/sciback_phy_10_2.pdf, 2010)

48- I. W. Frank, D. M. Tanenbaum, A. M. van der Zande, and P. L. McEuen, Mechanical properties of suspended graphene sheets, J. Vac. Sci. Technol. B 25(6) (2007).

49- W. Thomson, On the electro-dynamic qualities of metals: Effects of magnetization on the electric conductivity of nickel and of iron, Proc. R. Soc. London, Vol. 8, 546–550 (1856).

50- W. Thomson, On the electro-dynamic qualities of metals: Effects of magnetization on the electric conductivity of nickel and of iron, Proc. R. Soc. London, Vol. 8, 546–550 (1856).

51- P. W. Bridgman, Some properties of single metal crystals, Proc. Nat. Acad. Sci. U.S.A, Vol. 10, 411–415 (1924).

52- H. A. Nielsen, From Locomotives to Strain Gages, New York: Vantage Press (1985).

53- H. A. Nielsen, From Locomotives to Strain Gages. New York: Vantage Press, 1985.

54- K. E. Petersen, Silicon as a mechanical material, Proc. IEEE, Vol. 70, 420–457 (1982).

55- O. Paul, J. Gaspar, and P. Ruther, Advanced silicon microstructures, sensors, and systems, IEEJ Trans., Vol. 2, 199–215 (2007).

56- A. A. Barlian, W. T. Park, J. R. Mallon, A. J. Rastegar, and B. L. Pruitt, Review: Semiconductor piezoresistance for Microsystems, Proceeding of the IEEE, Vol. 97, No. 3, 513-552 (2009).

57- H. Rolnick, Tension coefficient of resistance of metals, Phys. Rev., Vol. 36, 506–512 (1930).

58- L. Fang, W. L. Wang, P. D. Ding, K. J. Liao, and J. Wang, Study on the piezoresistive effect of crystalline and polycrystalline diamond under uniaxial strains, J. Appl. Phys., Vol. 86, 5185 (1999).

59- M. Aslam, I. Taher, and A. Masood, M. A. Tamor and T. J. Potte, Piezoresistivity in vapor-deposited diamond films, Appl. Phys. Lett., Vol. 60, No. 23, (1992).

60- M. R. Werner and W. R. Fahrner, Review on materials, microsensors, systems and devices for high-temperature and harsh-environment applications,Industrial Electronics, IEEE Trans., Vol. 48, 249–257,(2001).

61- M. Werner, G. Kro¨tz, H. Mo¨ller, M. Eickhoff, P. Gluche, M. Adamschik, C. Johnston, and P. R. Chalker, High Temperature sensors based on SiC and diamond technology, Sensors Update, Vol. 5, 141–190 (1999).

62- M. P. D'Evelyn, D. E. Slutz, and B. E. Williams, Elastic properties of CVD diamond via dynamic resonance measurements, in Materials Research Society Symposium, San Francisco, CA, 115–120 (1995).

63- M. Werner, P. Gluche, M. Adamschik, E. Kohn, and H.-J. Fecht, Review on diamond based piezoresistive sensors, in Industrial Electronics, Proceedings. ISIE '98. IEEE International Symposium, Vol. 1, 147–152, (1998).

64- S. Sahli, Ultra-high sensitivity intra-grain poly-diamond piezoresistors, Sensors and Actuators. A, Physical, Vol. 71, 193 (1998).

65- J.-P. Salvetat, A. J. Kulik, J.-M. Bonard, G. A. D. Briggs, T. Stockli, K. Metenier, S. Bonnamy, F. Beguin, N. A. Burnham, and L. Forro, Elastic modulus of ordered and disordered multiwalled carbon nanotubes, Advanced Materials, Vol. 11, 161–165 (1999).

66- H. Dai, Carbon nanotubes: Opportunities and challenges, Surf. Sci., Vol. 500, 218–241 (2002).

67- G. T. A. Kovacs, Micromechanical transducers sourcebook (McGraw-Hill, New York 1998)

68- T. J. Chung, Applied Continuum Mechanics, (Cambridge University Press 1996).

69- A. N. Cleland, Foundations of Nanomechanics, (springer 2003).

70- I. H. Shames, Mechanics of deformable solids, (Prentice–Hall, Englewood Cliffs, N.J., 1964).

71- J. Turley, and G. Sines, The anisotropy of Young's modulus, shear modulus and Poisson's ratio in cubic materials, J. Phys. D 4, 264 (1971).

72- L. D. Landau, and E. M. Lifshitz, Theory of elasticity (Butterworth-Heineman, 1986).

73- P. Liu, and Y. W. Zhang, Temperature-dependent bending rigidity of graphene, Appl. Phys. Lett., Vol. 94, 231912 (2009).

74- B. I. Yakobson, C. J. Brabec, and J. Bernholc, Nanomechanics of Carbon Tubes: Instabilities beyond Linear Response, Phys. Rev. Lett., Vol. 76, 2511 (1996).

75- A. H. Castro Neto, F. Guinea, N. M. R. Peres, K. S. Novoselov, and A. K. Geim, The electronic properties of graphene, Rev.Mod. Phys., Vol. 81, 109 (2009).

76- J. Atalaya, A. Isacsson, and J. M. Kinaret, Continuum Elastic Modeling of Graphene Resonators, Nano Lett., Vol. 8, 4196 (2008).

77- R. Faccio, P. A. Denis, H. Pardo, C. Goyenola, and A. W. Mombru, Mechanical properties of graphene nanoribbons, J. Phys.: Condens.Matter, Vol. 21, 285304 (2009).

78- A. C. Ferrari, J. C. Meyer, V. Scardaci, C. Casiraghi, M. Lazzeri, F. Mauri, S. Piscanec, D. Jiang, K. S. Novoselov, S. Roth, and A. K. Geim, Raman Spectrum of Graphene and Graphene Layers, Physical Review Letters, Vol. 97, 187401 (2006).

79- A. Gupta, G. Chen, P. Joshi, S. Tadigadapa, and P.C. Eklund, Raman Scattering from High-Frequency Phonons in Supported n-Graphene Layer Films, Nano Letters, Vol. 6, No. 12, 2667-2673 (2006).

80- S. Roddaro, P. Pingue, V. Piazza, V. Pellegrini, and F. Beltram, The optical visibility of graphene: interface colors of ultrathin graphite on SiO_2, Nano Letters, Vol. 7, No. 9, 2707-2710 (2007).

81- M. Lafkioti, B. Krauss, T. Lohmann, U. Zschieschang, H. Klauk, K. v. Klitzing, and J.n H. Smet, Graphene on a Hydrophobic Substrate:Doping Reduction and Hysteresis Suppression under Ambient Conditions,Nano Letters, Vol. 10, 1149-1153 (2010).

82- Grégory F. Schneider, Victor E. Calado, Henny Zandbergen, Lieven M.K. Vandersypen and Cees Dekker, Wedging Transfer of Nanostructures, *Nano Lett.*, Vol. **10** (5), 1912–1916 (2010).

83- P. Blake, E. W. Hill, A. H. Castro Neto, K. S. Novoselov, D. Jiang, R. Yang, T. J. Booth, and A. K. Geim, Making graphene visible, Applied Physics Letter, Vol. 91, 063124 (2007).

84- B. Stegemann, H. Backhaus, H. Kloss, and E. Santner, Spherical AFM Probes for Adhesion Force Measurements on Metal Single Crystals, Modern Research and Educational Topics in Microscopy , 820-827 (2007)

85- B. Bhushan, Nanotribology and nanomechanics, Progress in Surface Science, Vol. 41, 3-49, (2005).

86- Scanning Probe microscope training notebook, (Vecco Instrument Inc. 2003).

87- E. Meyer, Atomic force microscopy, Progress in Surface Science, Vol. 41, 3-49 (1992).

88- Y. Song and B. Bhushan, Atomic force microscopy dynamic modes: modeling and applications, Condens. Matter, Vol. 20, 225012 (2008).

89- D. Norouzi, M. M. Mueller, and M. Deserno, How to determine local elastic properties of lipid bilayer membranes from atomic-force microscope measurements: A theoretical analysis, Phys. Rev. E., Vol. 74, 061914 (2006).

90- V. Shahin, Y. Ludwig, C. Schafer, D. Nikova and H. Oberleithner, lucocorticoids remodel nuclear envelope structure and permeability, Cell Science,Vol. 118, 2881-2889 (2005).